

1 **Transient histone deacetylase inhibition induces cellular memory of
2 gene expression and three-dimensional genome folding**

3
4 Flora Paldi¹, Michael F Szalay¹, Marco Di Stefano¹, Daniel Jost², Hadrien Reboul¹ and
5 Giacomo Cavalli^{1*}

6
7 ¹ Institute of Human Genetics, CNRS and University of Montpellier, France
8 ² Laboratoire de Biologie et Modélisation de la Cellule, École Normale Supérieure de Lyon,
9 CNRS, UMR5239, Inserm U1293, Université Claude Bernard Lyon 1

10
11 *Correspondence: giacomo.cavalli@igh.cnrs.fr

12
13 **Abstract**

14 Epigenetic memory enables the stable propagation of gene expression patterns in response
15 to transient developmental and environmental stimuli. Although three-dimensional (3D)
16 organisation is emerging as a key regulator of genome function, it is unknown whether it
17 contributes to cellular memory. Here, we establish that acute perturbation of the epigenome
18 can induce cellular memory of gene expression in mouse embryonic stem cells (mESCs).
19 Specifically, we uncover how a pulse of histone deacetylase inhibition translates to changes
20 in histone acetylation and methylation, as well as global and local genome folding. While most
21 epigenomic and transcriptional changes are readily reversible once the perturbation is
22 removed, genome architecture partially maintains its perturbed conformation. This is
23 significant, as a second transient pulse of hyperacetylation induces continued gene
24 expression deregulation at hundreds of loci. Using ultra-deep Micro-C, we associate memory
25 of gene expression with enhancer-promoter contacts and repressive chromatin topology
26 mediated by Polycomb. These results demonstrate how cells are able to record a transient
27 stress in their 3D genome architecture, enabling them to respond more robustly in a second
28 bout of the same perturbation.

29

30
31 Cellular identity is established by gene regulation and epigenetic mechanisms that
32 shape the transcriptional landscape. The information to maintain transcriptional programs is
33 stored in alternative chromatin states that provide the means for cellular plasticity to respond
34 to developmental and environmental cues. This is particularly true for embryonic stem cells
35 (ESCs) that have the developmental potential to give rise to all germ layers. ESCs have
36 distinctive permissive chromatin where activating and repressive configurations often co-
37 exist¹. These bivalent or poised states are mainly established around developmental genes
38 and require a fine balance between opposing signals to keep gene expression sufficiently low
39 but also prime genes for future activation^{2,3}. An important feature of functional chromatin states
40 is the ability to convert short-lived signals to long-lived changes in gene expression – a concept
41 commonly referred to as cellular memory⁴. Cellular memory is widely accepted as an important
42 aspect underlying development and often involves a complex interplay between different
43 epigenetic layers to stabilize gene expression programs following cellular state transitions⁵.
44 However, the crosstalk between epigenetic mechanisms and to what extent can they
45 contribute to memory have been difficult to study due to functional redundancy between
46 components of the epigenetic machinery, as well as the lack of experimental approaches that
47 uncouple gene regulation from cellular memory.

48 In this study we sought to understand the dynamics of the epigenome during a short-
49 lived disruption of chromatin state balance. To this end, we pulsed mouse ESCs with the
50 histone deacetylase (HDAC) inhibitor trichostatin A (TSA)⁶ that has rapid, global, yet reversible
51 effects on histone acetylation. This latter aspect was critical for allowing us to ask whether
52 such an acute perturbation could trigger cellular memory on the short term. Using a
53 combination of RNA sequencing (RNA-seq), chromatin immunoprecipitation followed by
54 sequencing (ChIP-seq) and ultra-deep Micro-C, we investigate the interplay of gene
55 expression, histone landscape and genome folding at an unprecedented resolution. We place
56 particular emphasis on 3D genome organisation, which is emerging as a key contributor to
57 cellular identity through its role in gene expression control⁷, and we uncover a novel link
58 between 3D genome organisation and cellular memory.

59

60 **Results**

61

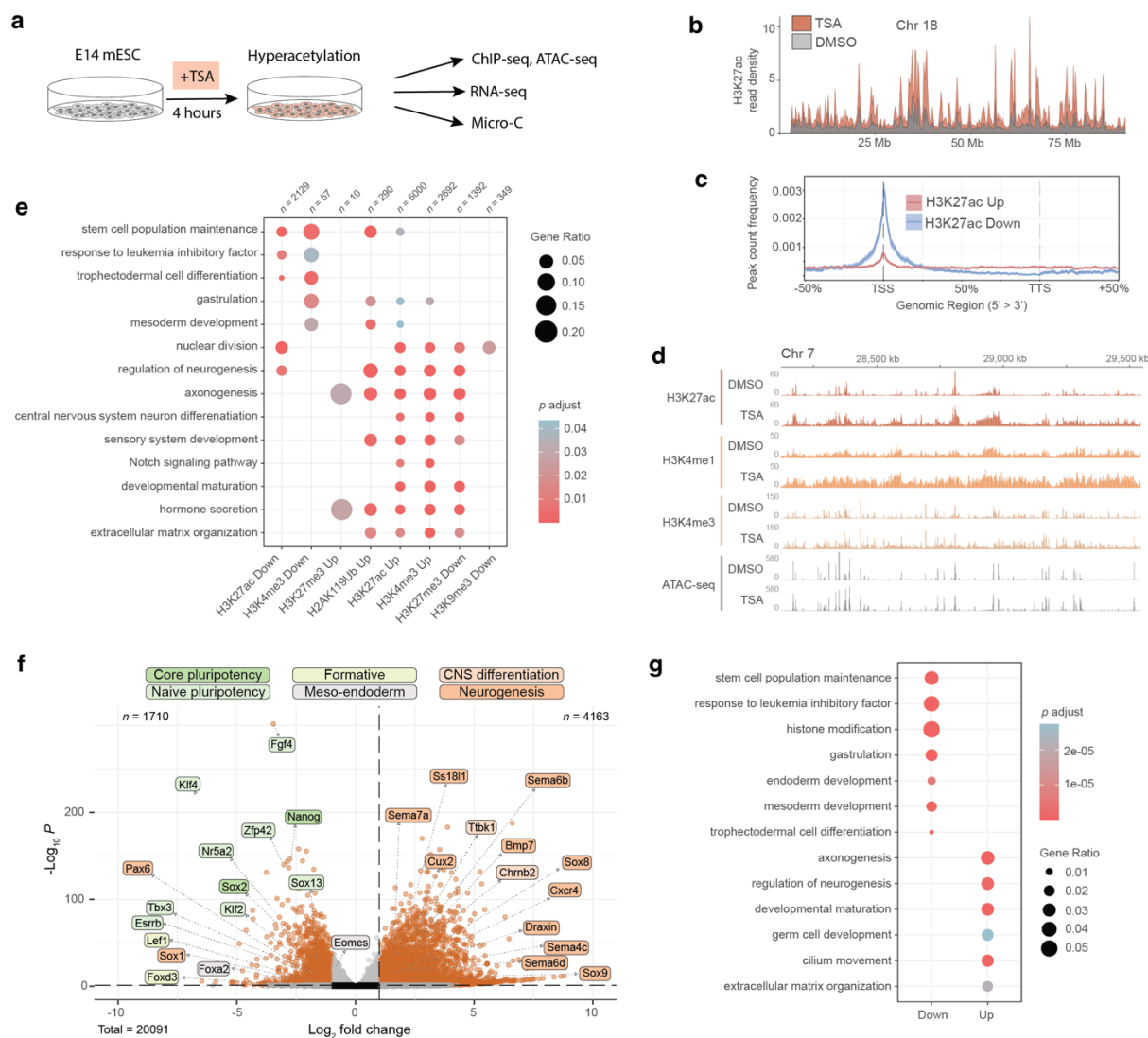
62 **A HDAC inhibition pulse leads to global changes in the histone landscape and gene 63 expression**

64 To disrupt the chromatin state balance of mESCs, we pulsed them with TSA for 4 hours
65 (Fig. 1a). To avoid pleiotropic effects, we optimised treatment conditions so that histone
66 hyperacetylation is induced (Extended Data Fig. 1a-b) but the bulk of the acetylome, cell cycle
67 progression and cell viability remain unchanged (Extended Data Fig. 1c-d). Calibrated ChIP-
68 seq indicated that acute TSA treatment efficiently induced genome-wide H3K27
69 hyperacetylation (Fig. 1b) resulting in significant increase in H3K27ac signal at >30,000 sites
70 (Extended Data Fig. 1e). We also detected ~2,800 previously strong H3K27ac peaks that
71 showed modestly decreased but dispersed signal enrichment upon TSA treatment. While
72 H3K27ac loss was highly specific to TSSs, H3K27ac gain occurred ubiquitously around *cis*-
73 regulatory elements, along gene bodies as well as in intergenic regions (Fig. 1c, Extended
74 Data Fig. 1f).

75 As functional chromatin states are maintained by an interplay between active and repressive
76 histone modifications^{5,8}, we next focused on characterising secondary changes in the histone
77 landscape. By categorising genomic intervals as active (enriched in H3K27ac, H4K4me1 or
78 H3K4me3) and repressive (enriched in H3K9me3, H3K27me3 or H2AK119Ub), we found that
79 TSA treatment caused a larger fraction of the genome to be in an active state, while repressive
80 intervals decreased nearly 2-fold (Extended Data Fig. 1g). Indeed, we identified thousands of
81 differential peaks for all examined histone modifications, where activating marks were in
82 general gaining signal and repressive marks underwent mostly loss of enrichment (Fig. 1d,
83 Extended Data Fig. 1f). Gene annotation of differential ChIP-seq peaks pointed to an
84 amplification of developmental processes and a suppression of pluripotency (Fig. 1e).

85 Next, we carried out bulk RNA-seq to discern whether the effects of HDAC inhibition on the
86 transcriptome reflect the changes we detect in the histone landscape. As HDAC1 is an
87 important regulator of early development^{9,10}, we focused on transcriptional changes related to
88 ESC identity. As suggested by reorganisation of the histone modification landscape,
89 downregulated genes were associated with stem cell population maintenance as well as
90 endoderm and mesoderm development (Fig. 1f-g). In parallel, we observed upregulation of
91 genes associated with developmental maturation, in particular specification of the neural
92 lineage as previously described¹⁰⁻¹³.

93 In sum, we found that acute HDAC inhibition leads to widespread accumulation of
94 H3K27ac and global changes in the histone modification landscape that promote a gene
95 expression programme associated with exit from pluripotency.



96

97

98 **Figure 1 – Acute HDAC inhibition leads to global changes in the histone landscape and**
99 **gene expression.** **a**, E14 mESCs were pulsed for 4 hours with Trichostatin A (TSA) and
100 assayed for changes in chromatin states by a combination of ChIP-seq, ATAC-seq, RNA-seq
101 and Micro-C. **b**, Plot showing H3K27ac ChIP-seq read density on chromosome 18 (bin size =
102 10 kb). **c**, Differential H3K27ac peak count frequency distribution relative to gene bodies (TSS
103 = transcription start site, TTS = transcription termination site). Shading represents 95%
104 confidence interval (CI). **d**, Genomic snapshot of spike-in normalised ChIP-seq and ATAC-seq
105 signal over a typical hyperacetylated region. **e**, Gene Ontology enrichment of terms related to
106 development among genes located within 1 kb distance from differential ChIP-seq peaks. **f**,
107 Volcano plot showing differential gene expression (significance cutoffs: adjusted p-value >
108 0.05, absolute log₂ fold change > 1) upon TSA treatment. Labels correspond to core and naïve
109 pluripotency, formative, meso-endodermal, central nervous system (CNS) differentiation and
110 neurogenesis marker genes. **g**, Gene Ontology enrichment of terms related to development
111 among up- and down-regulated genes.

112

113 Global and fine-scale architectural changes characterise the TSA chromatin state

114

115 Imaging studies have shown that TSA treatment leads to chromatin decompaction both
116 at global^{14,15} and local^{15,16} scales. To understand how these alterations translate to changes in
117 chromatin contacts, we generated ultra-deep Micro-C contact maps with 8.5 and 6.6 billion
118 unique valid 3D chromatin contacts for control (DMSO) and TSA conditions respectively
119 (Supplementary Table 1). Our datasets show more uniform genomic coverage over both active
120 and inactive genomic intervals with respect to previous Micro-C studies^{17,18}, and provide
121 unbiased genome-wide interaction maps with unprecedented detail (Extended Data Fig. 2a-
122 b). Unlike recent high-resolution capture studies, we do not observe microcompartments at
123 previously described loci¹⁹, only mild on-diagonal insulation at microcompartment anchor sites.
124 We attribute the differences in our dataset to differences in Micro-C protocol rather than to
125 insufficient data depth (Extended Data Fig. 2c-d).

126

127 When we compared contact maps generated from control and TSA-treated cells, we detected
128 a dramatic increase in *trans* contacts upon TSA treatment (Extended Data Fig. 3a). This was
129 concomitant with a marked decrease in *cis* interactions at nearly all genomic distances
130 (Extended Data Fig. 3b). TSA treatment also led to a loss of prominent A compartment
131 interactions - a characteristic of embryonic stem cells²⁰ - without major changes in
132 compartment identity (Fig. 2a, Extended Data Fig. 3c). While *trans* contacts were gained in
133 both compartments (Extended Data Fig. 3d), BB interactions - a feature of differentiated cells²⁰
134 - became prominent in *cis*. This observation prompted us to examine if A and B compartments
135 were asymmetrically impacted by TSA treatment. Indeed, gain in activating histone marks in
136 A compartment exceeded that in B, and most gene expression deregulation corresponded to
137 TSSs located in the A compartment (Fig. 2b-c, Extended Data Fig. 3e).

138

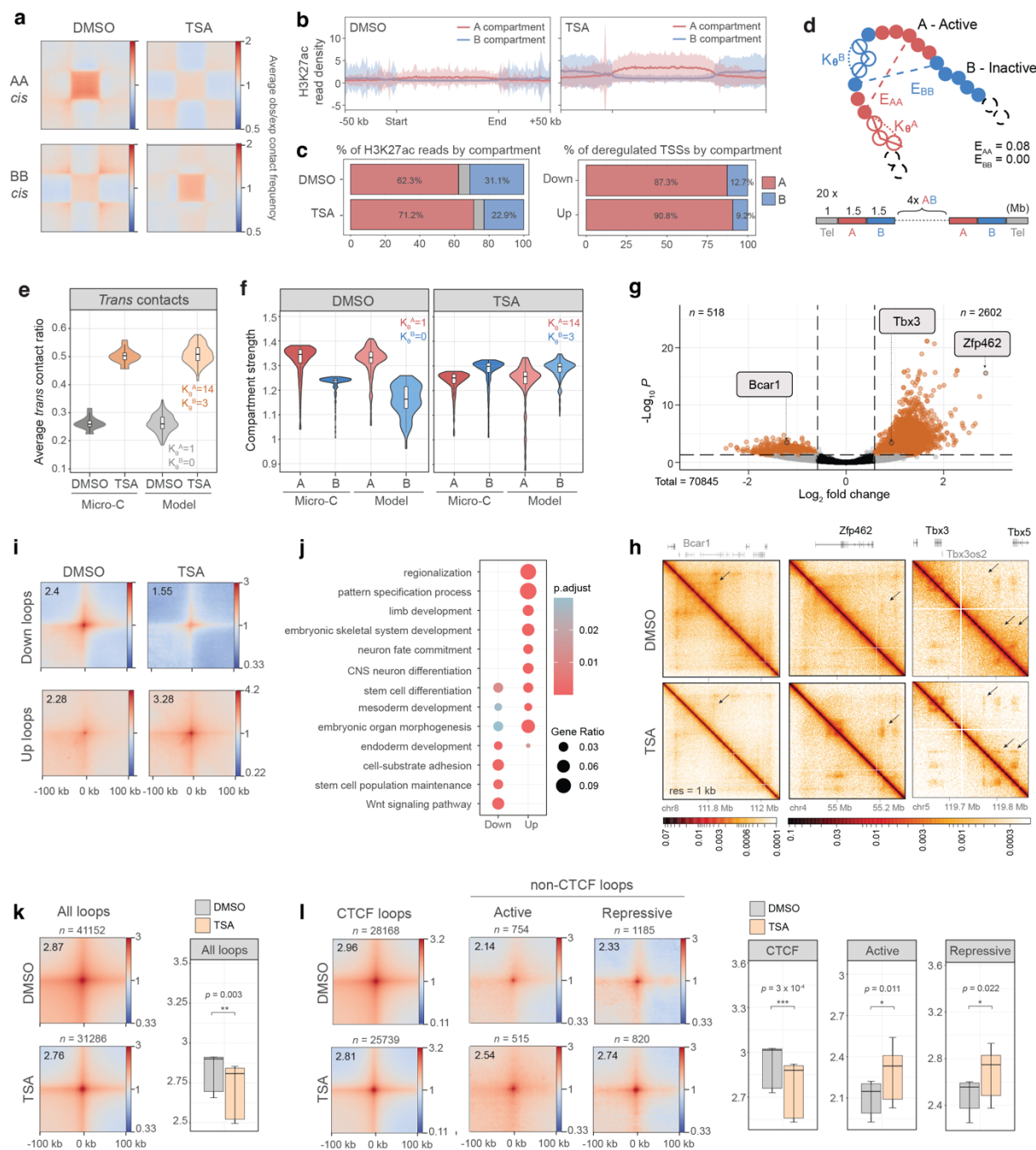
139 It has been previously suggested that elevated transcriptional activity or acetylation level
140 increases the stiffness of the chromatin fibre, leading to an increase in *trans* interactions²¹ and
141 chromosome reorganisation²². We tested this idea by simulating TSA-induced changes on
142 global chromatin folding using mechanistic 3D polymer modelling²³. First, we used a single-
143 chain block copolymer model (Fig. 2d) made of A and B chromatin regions to infer self-
144 attraction energies (E_{AA} , E_{BB}) that best reproduce the A/B compartment strength in DMSO
145 condition (Extended Data Fig. 3f-g, Methods). Since A and B compartments are
146 asymmetrically²² affected by TSA-induced hyperacetylation and transcriptional upregulation
147 (Fig. 2b, c), we then simulated the effect of TSA treatment by changing the stiffness

148 differentially within A and B domains in a multi-chain system. By optimising the value of
149 stiffness to match the median *trans*-interaction ratio (Fig. 2e, Extended Data Fig. 3h-j), the
150 TSA conformation was compatible with an increase of stiffness in A-domains to a greater
151 degree than in B-domains ($K_{\theta A} = 14 K_{\theta}$, versus $K_{\theta B} = 3.0 K_{\theta}$). Interestingly, the change in
152 stiffness we applied to reproduce the *trans*-contact ratio automatically predicted the swap in
153 compartment strength without modifying the A-A and B-B attraction energies (Fig. 2f, Extended
154 Data Fig. 3i): A-domains lost compartment strength while B-domains gained it, so that in TSA
155 B-B interactions were stronger than A-A. Additionally, our model predicted a displacement of
156 A-domains towards the periphery of the simulated spherical nucleus²⁴ (Extended Data Fig.
157 3k).

158 Subsequently, we sought to comprehensively map conformational changes that occur at the
159 submegabase scale. Whole genome analyses identified >3000 focal interactions with
160 differential looping strength (Fig. 2g-i) that were strongly associated with developmentally
161 important loci (Fig. 2j, Extended Data Fig. 2l). As we detected nearly 3500 CTCF peaks that
162 became stronger in TSA, we tested whether increase in loop strength was due to increased
163 CTCF binding (Extended Data Fig. 2m). Contrarily, we found that CTCF-mediated loops
164 globally became weaker. Instead, non-CTCF loops – carrying either active (H3K27ac,
165 H3K4me1, H3K4me3) or repressive (H3K9me3, H3K27me3, H2AK119Ub) chromatin
166 signatures – became stronger upon TSA treatment (Fig. 2k-l).

167

168 Taken together, TSA treatment had a profound effect on global genome folding,
169 promoting inter-chromosomal contacts and decreasing A-A compartment interactions. These
170 changes in global chromatin folding were compatible with a compartment-specific increase of
171 stiffness of the chromatin fibre in our biophysical modelling simulations. In parallel, TSA
172 treatment caused specific, fine-scale restructuring where CTCF-dependent and epigenetic-
173 state driven loops behaved differently. Importantly, annotation of sites with rewired chromatin
174 contacts mirrors ongoing developmental processes that we identified from changes in the
175 transcriptome and the histone landscape.



176

177

178 **Figure 2 – Global and fine-scale architectural changes characterise the TSA chromatin**
 179 **state.** **a**, Aggregate plots of homotypic interactions between A and B compartments in *cis*.
 180 **b**, Metaplots showing H3K27ac normalised ChIP-seq read density over A and B compartments
 181 (bin size = 1 kb). Shading represents standard deviation. **c**, Distribution of H3K27ac ChIP-seq
 182 reads (left panel) and up- and down-regulated TSSs (right panel) by compartment. **d**,
 183 Schematic representation of biophysical modelling where E_{AA} and E_{BB} correspond to the
 184 attraction energies and K_e^A and K_e^B correspond to the stiffness of the chromatin fibre, in A and
 185 B domains, respectively. Each chromosome was modelled by a 20 Mb chain where each bead
 186 represents 5 kb of DNA. A and B domains were set at 1.5Mb in size to match the mean

187 compartment size derived from the Micro-C data, resulting in 6 A-domains, 6 B-domains, and
188 2 telomeric regions of 1 Mb each at the extremities for the chain. A nucleus was modelled
189 using 20 chains. **e**, *Trans* contact ratio in DMSO and TSA in the Micro-C data and in the model.
190 **f**, Compartment strength in DMSO (left panel) and TSA (right panel) in the Micro-C data and
191 in the model. **g**, Volcano plot of differential loops between DMSO and TSA (significance
192 cutoffs: adjusted p -value > 0.05 , absolute fold change > 1.5). Positive \log_2 fold change
193 indicates stronger interaction in TSA. **h**, Contact maps showing differential looping at the
194 *Bcar1*, *Zfp462* and *Tbx3* loci. **i**, Aggregate plots of Micro-C signal around differential loops at
195 4 kb resolution. **j**, Gene Ontology enrichment among genes closest to differential loop anchors.
196 **k**, Pile-ups showing Micro-C signal around all loops identified in DMSO (top) and TSA (bottom)
197 (resolution = 4 kb). Quantification of aggregate loop signal is shown on the right (paired two-
198 tailed t-test; ** $p < 0.01$). Data shown are the median, with hinges corresponding to interquartile
199 range (IQR) and whiskers extending to the lowest and highest values within $1.5 \times$ IQR. **l**, Pile-
200 ups of Micro-C signal around loops stratified by the presence (CTCF loops) or absence (non-
201 CTCF loops) of CTCF ChIP-seq peaks at loop bases (resolution = 4 kb). Non-CTCF loops
202 have been further divided to active and repressive based on the presence of activating
203 (H3K27ac, H3K4me1) or repressive (H3K27me3, H3K9me3) ChIP-seq signal at loop bases.
204 Quantification of aggregate loop strength is shown on the right (paired two-tailed t-test; * $p <$
205 0.05, *** $p < 0.001$). Data shown are the median, with hinges corresponding to IQR and
206 whiskers extending to the lowest and highest values within $1.5 \times$ IQR.

207

208 **Changes in histone modification landscape and chromatin looping underlie differential 209 gene expression**

210

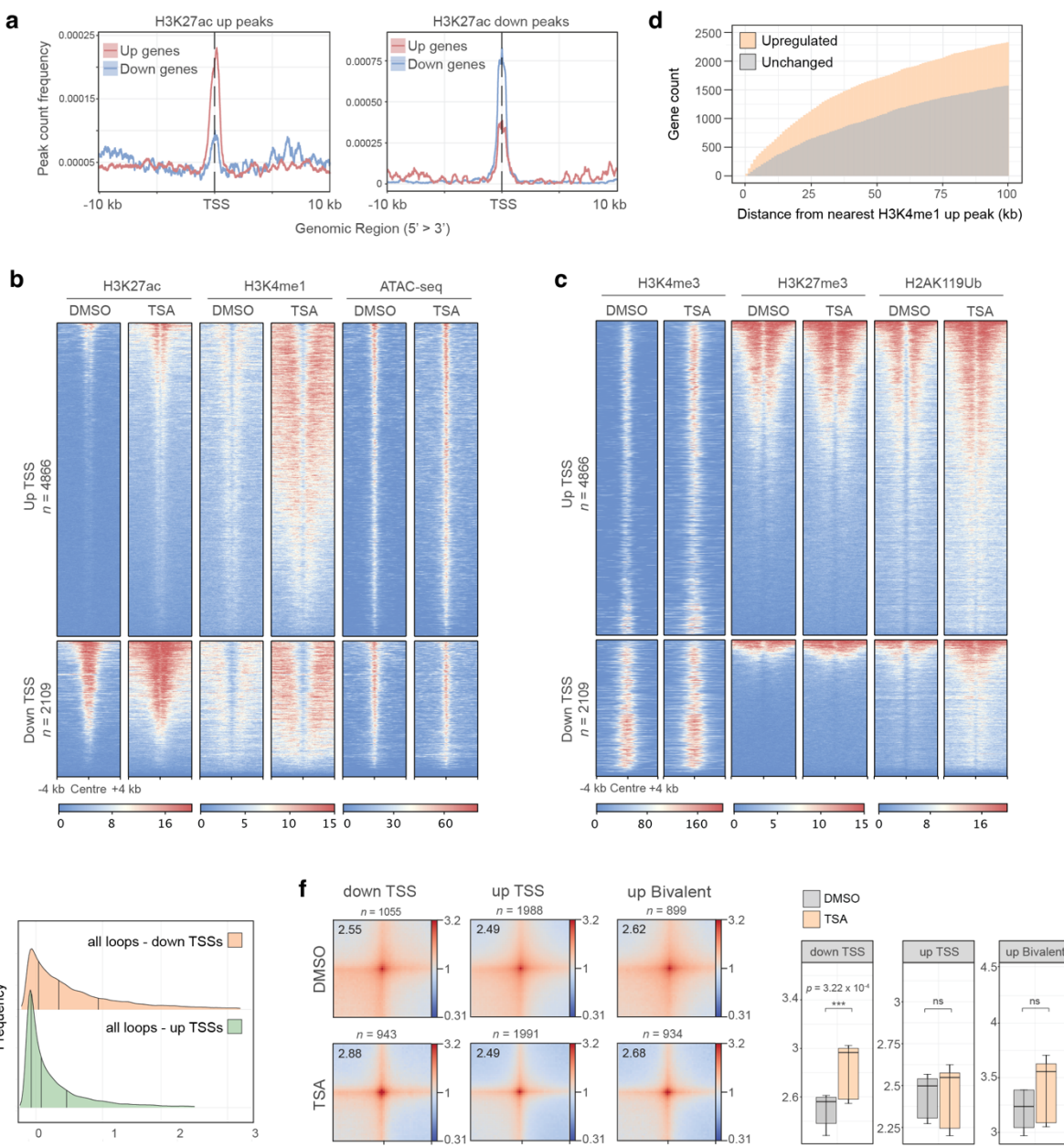
211 We next asked what epigenomic changes underlie TSA-induced gene expression
212 deregulation. As upregulated TSSs were enriched for H3K27ac peaks that gain signal in TSA,
213 whereas peaks that showed decreased signal were more frequently localised to
214 downregulated TSSs (Fig. 3a), we conclude that transcriptomic changes are least partially
215 correlated to changes in the H3K27ac landscape. Analyses of epigenetic signatures around
216 upregulated TSSs revealed that gain in H3K27ac was concomitant with a modest increase in
217 chromatin accessibility and a substantial gain of H3K4me1 in surrounding regions. (Fig. 3b)
218 On the other hand, we detected overlapping H3K4me3 and H3K27me3 signal at a large subset
219 of upregulated genes, indicating that bivalent genes are susceptible to TSA-mediated gene
220 derepression. This occurred with a gain in H3K4me3 and H3K27ac, but without a detectable
221 loss of H3K27me3 signal (Fig. 3c, Extended Data Fig. 4a).

222

223 To understand if transcriptional upregulation could be caused by ectopic enhancer activation,
224 we examined the linear proximity of genomic regions that gain H3K4me1 signal to gene
225 promoters. This revealed that such peaks form closer to upregulated gene promoters than
226 promoters of expression-matched control genes that do not undergo upregulation (Fig. 3d).
227 Similarly, upregulated TSSs were found to be in closer proximity to previously described
228 primed (H3K4me1+, H3K27ac-) and poised (H3K4me1+, H3K27me3+, H3K27ac-) enhancers^{25,26} (Extended Data Fig. 4b). As enhancer activation and subsequent gene
229 expression are often accompanied by the establishment of enhancer-promoter (E-P)
230 contacts^{20,27,28}, we analysed changes in chromatin looping associated with upregulated TSSs.
231 Although we detected an increased linear proximity of loops to upregulated TSSs, gene
232 expression upregulation seemingly occurred without noticeable changes in promoter contacts
233 (Fig. 3e-f).

235 Interestingly, we observed similar changes in the histone modification landscape at
236 downregulated TSSs, where active marks were gained in the absence of accumulation of
237 repressive histone modifications (Fig. 3a, d). Instead, even without TSA treatment a part of
238 downregulated TSSs were found to be strongly enriched for Myc and YY1 binding (Extended
239 Data Fig. 4c), transcriptional regulators that are direct targets of HDACs and whose acetylation
240 state has been described to modulate their molecular function^{29,30}. This suggests that TSA-
241 induced gene downregulation may be partially due to effects on non-histone targets of HDACs.
242 Crucially however, unlike upregulated TSSs, promoter loops around downregulated TSSs
243 became stronger (Fig. 3f). We noticed that around some of the most strongly downregulated
244 genes prominent *de novo* loops formed in TSA-treated cells. In these cases, looping was
245 globally associated with gene downregulation and occurred between existing H3K9me3 sites
246 with only a mild increase in H3K9me3 level (Extended Data Fig. 4d-h). This suggests that
247 repressive chromatin contacts could provide means for gene downregulation even when
248 activating histone modifications are acquired.

249 Altogether, we find that gene upregulation as well as downregulation occur with a gain of
250 activating chromatin marks. In general, while gene upregulation is potentially associated with
251 enhancer over-activation without gain in E-P contacts, downregulation is linked to repressive
252 chromatin looping.



253

254

255 **Figure 3 – Changes in histone landscape and chromatin looping underlie differential**
256 **gene expression.** **a**, H3K27ac up (left panel) and down (right panel) peak count frequency
257 distribution relative to TSSs of up- and down-regulated genes. Shading represents 95% CI. **b**,
258 H3K27ac, H3K4me1 and ATAC-seq signal around transcription start sites (TSS) of
259 differentially expressed genes. **c**, Heatmaps showing H3K4me3, H3K27me3 and H2AK119Ub
260 signal around TSSs of differentially expressed genes. **d**, Cumulative histogram showing
261 genomic distance between upregulated gene promoters and the nearest increased H3K4me1
262 peak. Control genes represent an expression-matched gene set that does not increase in
263 expression. **e**, Ridge plot showing the frequency of loop anchors in the function of genomic
264 distance from the nearest deregulated TSS. **f**, Aggregate plots of Micro-C signal around loops

265 where anchors overlap with down- (left) or up-regulated (middle) TSSs, as well as bivalent
266 (right) TSSs that undergo upregulation (resolution = 4 kb). Quantification of piled-up loop
267 signal is shown on the right (paired two-tailed t-test; ns > 0.05, ***p < 0.001). Data shown are
268 the median, with hinges corresponding to IQR and whiskers extending to the lowest and
269 highest values within 1.5× IQR.

270

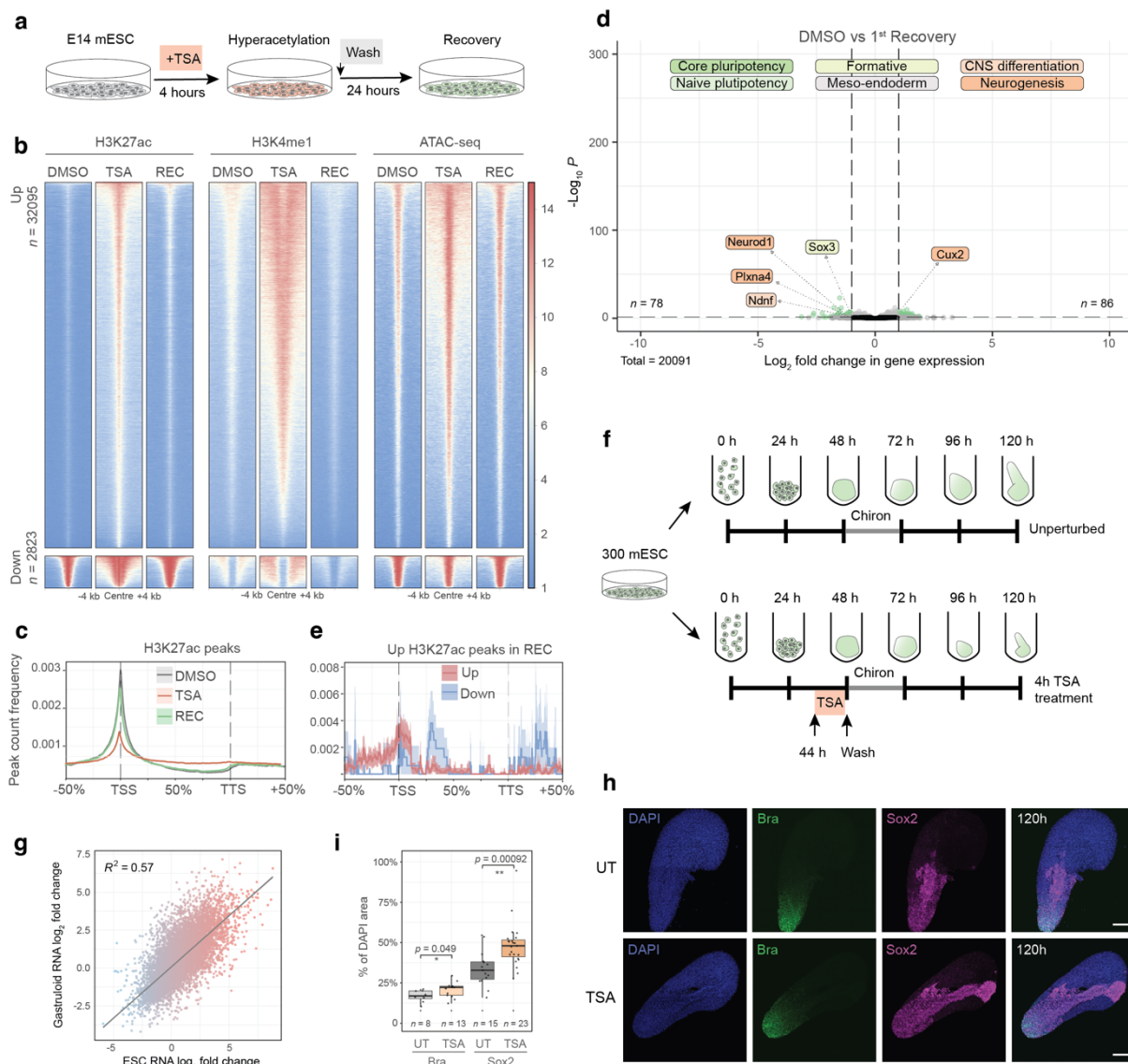
271 **ESCs recover their transcriptional identity and chromatin states following the removal
272 of HDAC inhibition**

273 Next, we asked if cells could revert to their unperturbed state upon TSA removal. We
274 postulated that if chromatin perturbation had strictly instructive roles, then the TSA cellular
275 state should be readily reversed once the perturbation is removed. Conversely, if the perturbed
276 chromatin state is a carrier of cellular memory, the changes should outlast the initial causative
277 event. To this end, we washed TSA-treated cells and let them recover for 24 hours, which
278 corresponds to approximately two cell doubling times. After 24 hours of TSA removal, original
279 H3K27ac levels and the rest of the acetylome appeared restored at the protein level (Fig. 4a,
280 Extended Data Fig. 1a-b), indicating successful removal of the perturbation. The effects of
281 TSA on the histone landscape were likewise readily reversible. Excess H3K27ac, H3K4me1
282 and chromatin accessibility were restored at once (Fig. 4b) and H3K27ac peaks re-gained
283 their enrichment around TSSs (Fig. 4c). Consistent with restoration of chromatin marks, TSA-
284 induced global transcriptional deregulation was nearly completely reversed with only a handful
285 of genes ($n = 164$) showing sustained changes (Fig. 4d). Even at these loci, transcription was
286 largely reversed, and only residual dysregulation persisted. Although we detected increased
287 H3K27ac level at certain genomic loci, these loci were not correlated with genes that remained
288 deregulated (Fig. 4e). Altogether, these data show that histone marks and gene expression
289 are almost entirely restored upon removal of TSA, showing little or no memory of the past
290 perturbation.

291 Importantly, the activity of the pluripotency network was efficiently recovered, and
292 developmental processes were downregulated anew. As mESC culture conditions are
293 designed to actively suppress differentiation, we were wondering if this efficient recovery was
294 a general feature of pluripotent cells, or whether it was due to culturing conditions that impose
295 such a dominant cell state that they overpower the effects of perturbations. To test this idea,
296 we grew mESCs into gastruloids^{31,32}, that we treated with TSA for 4 hours immediately prior to
297 the chiron pulse (Fig. 4f, Extended Data Fig. 5a, b). The effects of TSA on the transcriptome
298 strongly correlated between mESCs and gastruloids (Fig. 4g) with GO enrichment analysis
299 showing similar developmental deregulation in both conditions (Extended Data Fig. 5c).

300 Following washes - which restored H3K27ac within 24 hours (Extended Data Fig. 5c,d) - we
301 let control and TSA-treated cells develop for three days, until reaching a mature gastruloid
302 state. Gastruloids were then assayed for their transcriptomic and morphological features.
303 Interestingly, while the transcriptome was largely re-established, immunofluorescence staining
304 revealed morphological aberrations in TSA-treated (Extended Data Fig. 5e) gastruloids.
305 Although maintaining their ability to specify germ layers, we found that the TSA pulse led to a
306 marked expansion of the area staining positive for the neuroectodermal marker Sox2, while
307 the distribution of cells expressing the meso-endodermal marker Brachyury remained
308 unchanged (Fig. 4h-i).

309 In sum, mESC possess a remarkable capacity to recover their transcriptional and histone
310 modification landscape following a hyperacetylation pulse. Our findings in gastruloids fall in
311 line with these observations, namely that the effect HDAC inhibition on the transcriptome is
312 profound, but transcriptional recovery from it is nearly complete. Nevertheless, the incomplete
313 recovery of the Sox2 expression domain in gastruloids might indicate that a memory of the
314 TSA pulse might be ingrained.



315
316

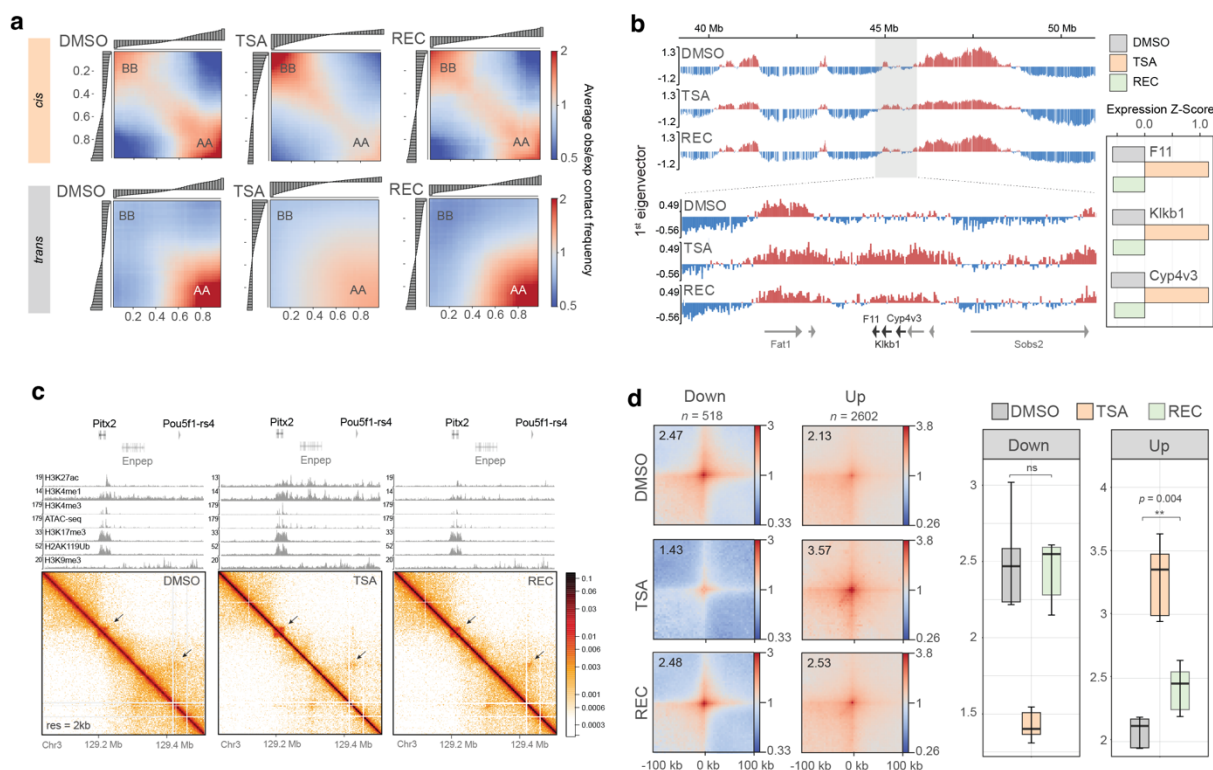
317 **Figure 4 – Pluripotent cells recover their transcriptional identity and chromatin states**
318 **following the removal of HDAC inhibition.** **a**, mESCs were washed extensively and were
319 re-assayed for their chromatin states 24 hours later. **b**, Heatmaps H3K27ac, H3K4me1 and
320 ATAC-seq signal in DMSO, TSA and recovery (REC) at differential H3K27ac peaks identified
321 in TSA. **c**, H3K27ac peak count frequency distribution in DMSO, TSA and recovery datasets
322 relative to gene bodies of all genes (TSS = transcription start site, TTS = transcription
323 termination site). Shading represents 95% CI. **d**, Volcano plot showing differential gene
324 expression 24 hours after TSA washout. Labels show developmental marker genes that
325 remain above the significance threshold (adjusted p-value > 0.05, absolute log₂ fold change >
326 1). **e**, H3K27ac peak count frequency distribution in recovery dataset relative to gene bodies
327 that remain up- and down-regulated (TSS = transcription start site, TTS = transcription
328 termination site). Shading represents 95% CI. **f**, Schematics of TSA treatment between 44 and
329 48 hours and subsequent washout during gastruloid differentiation. **g**, Scatterplot showing the

330 correlation of TSA-induced transcriptomic changes in mESCs and in 48-hour gastruloids.
331 Shading represents \log_2 fold change in mESCs. **h**, Representative images of Sox2 and
332 Brachyury immunostaining in 120-hour untreated gastruloids (top) or gastruloids 3 days
333 following transient TSA treatment (bottom) (scale bar = 100 μm). **i**, Quantification of Brachyury
334 (Bra) and Sox2 area over DAPI in 120 h gastruloids with and without TSA treatment. Data
335 shown are the median, with hinges corresponding to IQR and whiskers extending to the lowest
336 and highest values within 1.5 \times IQR (unpaired two-tailed t-test; * $p < 0.05$, *** $p < 0.001$).
337

338 **Genome architecture retains partial memory of the past conformation**

339 To further explore whether the TSA pulse could be recorded by mESCs, we analysed
340 3D genome folding upon restoration of the initial conditions. Surprisingly, we found that
341 chromatin conformation did not fully recover: the *cis-trans* ratio was restored only partially
342 (Extended Data Fig. 6a) and contact decay curves showed that *cis* contact depletion persisted,
343 particularly in the A compartment (Extended Data Fig. 6b). In terms of compartment
344 interactions, while AA interactions were efficiently recovered in *trans* and showed some
345 increase in *cis*, BB in *cis* interactions remained prominent following recovery from TSA (Fig.
346 5a). We could equally detect sustained changes in genome conformation at the gene level.
347 The depth of our data allowed us to carry out eigenvector decomposition at 4 kb resolution³³.
348 This revealed local instances where transcriptional and architectural recovery became
349 uncoupled. For example, gene expression upregulation at the F11, Klkb1 and Cyp4v3 loci in
350 TSA moved the ~200 kb long encoding genomic segment to the A compartment. Following
351 recovery, expression of all three genes was successfully restored, however the encoding
352 genomic segment had a continued A compartment identity, like in the TSA condition (Fig. 5b).
353 Additionally, incomplete architectural recovery was visible at certain genomic loci where
354 increased loop strength was maintained throughout the recovery period (Fig. 5c, Extended
355 Data Fig. 6c). Importantly, this occurred without any detectable, permanent changes in the
356 histone modification landscape. Finally, we found that globally, while differential loops that lost
357 strength in TSA were fully restored, loops that became stronger upon TSA treatment remained
358 enhanced (Fig. 5d).

359 In sum, we found that genome architecture carries a memory of its TSA-induced
360 conformation that is visible at the level of *cis* contact frequencies, compartment interactions
361 and at submegabase genome organisation.



362
363

364 **Figure 5 – Genome architecture retains partial memory of the past conformation. a,**
 365 Saddle plots of compartment interactions in *cis* (top panels) and in *trans* (bottom panels). **b,**
 366 High-resolution eigenvector tracks of the Micro-C data showing small-scale compartment
 367 switch around the F11-Klkb1-Cyp4v3 loci that persists in recovery. Gene expression Z-Score
 368 is shown in the right. **c,** Micro-C maps at the Pitx2 locus showing incomplete architectural
 369 recovery. ChIP-seq tracks of the corresponding condition are shown above. **d,** Pile-ups of
 370 Micro-C signal around differential loops in DMSO, TSA and recovery (resolution = 4 kb).
 371 Quantification of piled-up loop signal is shown on the right (paired two-tailed t-test; ns > 0.05,
 372 **p < 0.01). Data shown are the median, with hinges corresponding to IQR and whiskers
 373 extending to the lowest and highest values within 1.5× IQR.

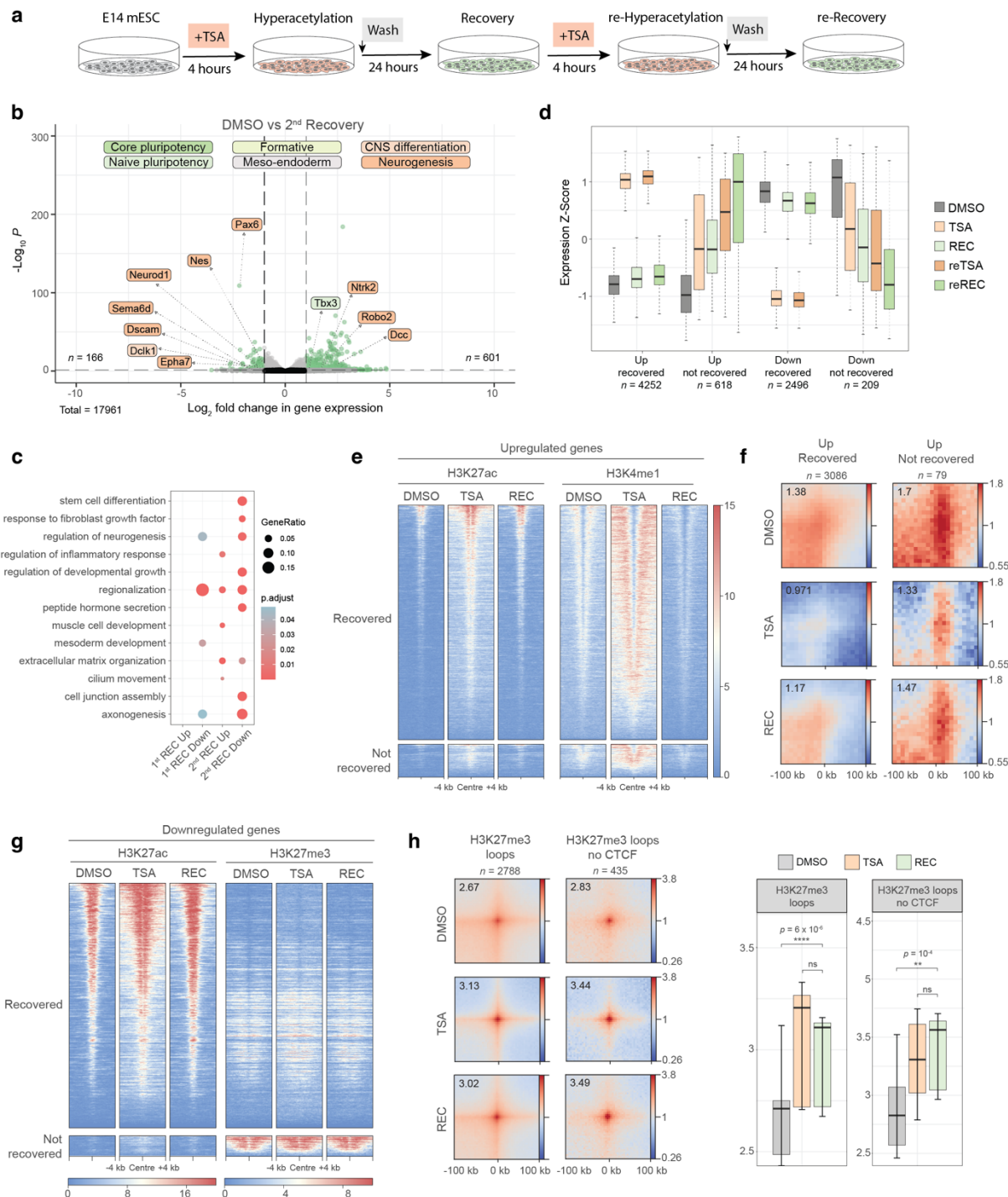
374
375 **Sustained gene expression deregulation is associated with strong regulatory 3D
376 contacts**

377 We next reasoned that if the persisting minor architectural and transcriptional changes
 378 signified cellular memory, then repeated exposure to TSA should have more severe
 379 consequences. To test this hypothesis, we subjected mESCs to a second cycle of TSA
 380 treatment and recovery (Fig. 6a) which, similarly to the first, did not compromise cell viability
 381 or cell cycle progression (Extended Data Fig. 1a-d). Crucially, while the effects of the second
 382 TSA treatment were comparable to the first (Extended Data Fig. 7a, b), recovery from the

384 second treatment was less complete (Fig. 6b). Hundreds of genes remained strongly
385 deregulated ($n = 767$) and showed association with developmental processes, suggesting that
386 the second pulse of perturbation had a greater impact on cellular identity (Fig. 6c). Next, we
387 stratified differentially expressed genes based on their ability to recover from either TSA
388 treatments, and we plotted their expression over the double treatment course. This revealed
389 that, while most deregulated genes oscillated between their native and ectopic expression
390 states, a subset of genes showed progressively aggravating gene expression deregulation
391 (Fig. 6d), strongly indicative of cellular memory.

392 Finally, we aimed to decipher what distinguishes genes that recover from genes that retain
393 memory of their TSA-induced expression state. First, we analysed the histone modification
394 landscape around upregulated TSSs. This analysis showed no particular difference between
395 recovered genes and genes that did not recover: both groups were characterised by a gain of
396 activating histone marks which were efficiently restored during the first recovery (Fig. 6e).
397 Instead, a marked difference between the two gene groups was the presence of diffuse but
398 strong pre-existing E-P contacts at non-recovery genes compared to recovery genes (Fig. 6f,
399 Extended Data Fig. 7c). Next, similar TSS analyses among the downregulated genes revealed
400 that genes that did not recover were Polycomb targets, as indicated by abundant H3K27me3
401 signal around promoters (Fig. 6g). Interestingly, downregulation happened without an
402 apparent change in H3K27me3. Rather, we found that Polycomb loops gained substantial
403 strength at non-recovery TSSs (Extended Data Fig. 7d-e), as well as genome wide, both at
404 CTCF and CTCF-independent sites (Fig. 6h, Extended Data Fig. 7f). Critically, increased
405 Polycomb-mediated looping persisted following the first recovery period, without change in
406 H3K27me3 level at loop anchors (Extended Data Fig. 7h). Sustained loop strengthening was
407 a feature specific to Polycomb rather than repressive loops in general, as we found the *de*
408 *novo* H3K9me3 loops to recover efficiently (Extended Data Fig. 7g).

409 In conclusion, we found that repeated transient HDAC inhibition triggered cellular
410 memory of gene expression at a subset of genes. We associate memory with strong
411 architectural features surrounding deregulated TSSs: in case of upregulated genes prominent
412 pre-formed E-P contacts, at downregulated TSSs bolstered repressive Polycomb loops
413 perpetuate altered activity states. Importantly, these findings reveal a novel link between
414 cellular memory and genome architecture.



415 0 8 16 0 4 8
416
417 **Figure 6 – Sustained gene expression deregulation is associated with strong regulatory**
418 **3D contacts.** **a,** Following the recovery period, cells were exposed to a second TSA pulse,
419 wash and recovery cycle. **b,** Volcano plot showing differential gene expression (significance
420 cutoffs: adjusted p -value > 0.05 , absolute \log_2 fold change > 1) upon a second TSA (reTSA)
421 treatment. Labels correspond to core and naïve pluripotency, formative, meso-endodermal,
422 CNS differentiation and neurogenesis marker genes. **c,** Development-related Gene Ontology
423 term enrichment among genes that remain misregulated following the first and second

424 recoveries from TSA treatment. **d**, Gene expression Z-Scores of recovered and not recovered
425 genes through the TSA-recovery treatment course. Data shown are the median, with hinges
426 corresponding to IQR and whiskers extending to the lowest and highest values within 1.5×
427 IQR. **e**, H3K27ac and H3K4me1 ChIP-seq signal in DMSO, TSA, and Recovery at upregulated
428 TSS that recover (top) and do not recover (bottom). **f**, Pile-up of enhancer-promoter contacts
429 in DMSO, TSA and Recovery around upregulated TSS that recover (top) and do not recover
430 (bottom). **g**, H3K27ac and H3K27me3 ChIP-seq signal in DMSO, TSA, and Recovery at
431 downregulated TSS that recover (top) and do not recover (bottom). **h**, Aggregate plots Micro-
432 C signal in DMSO, TSA and Recovery at CTCF (left) and non-CTCF (right) loops with
433 H3K27me3 ChIP-seq signal at loops anchors (resolution = 4 kb). Quantification of piled-up
434 loop strength is shown on the right (paired two-tailed t-test; ns > 0.05, **p < 0.01. ****p <
435 0.0001). Data shown are the median, with hinges corresponding to IQR and whiskers
436 extending to the lowest and highest values within 1.5× IQR.

437

438 **Discussion**

439

440 The interplay between epigenetic layers and whether they function synergistically or
441 antagonistically remains an area of active research. The findings presented in this study
442 describe a crosstalk between activating and repressive epigenetic modifications, as well as
443 genome folding, that profoundly modulate the mESC transcriptional programme. Namely, we
444 uncover how acute perturbation of the histone acetylation landscape rapidly translates to
445 changes in the histone methylation landscape and 3D chromatin organisation. Although the
446 majority of epigenomic changes are reversible, we find that certain alterations in 3D genome
447 folding persist and associate to a transcriptional memory effect at a subset of genomic loci.

448 Besides the general opening and activation of chromatin at promoters, we find widespread
449 H3K4me1 deposition upon TSA treatment, indicating the deployment of new enhancers.
450 These are likely to be major drivers of gene upregulation as previous studies have shown that
451 the enhancer landscape – rather than promoter activity – is more significant for lineage
452 determination^{34,35}. Accordingly, enhancers are the most epigenetically dynamic regions of the
453 genome^{36,37}, explaining their susceptibility to the disruption of chromatin state balance.
454 Interestingly, we find that H3K27 acetylation can trigger H3K4me1 deposition, which questions
455 the commonly accepted sequence of events in enhancer activation where H3K4me1 is
456 supposed to precede H3K27ac^{38,39}. Once activated, the maintenance of enhancer activity is
457 an active process⁴⁰⁻⁴², explaining the efficient recovery of the enhancer landscape and
458 transcriptional programme once the acetylation landscape is restored. Interestingly, we find

459 that gene upregulation occurs without changes in E-P contacts, which agrees with recent
460 studies that, in many instances, uncouple gene activation from a need to increase the
461 frequency of physical contact^{43–45}, or find that they are coupled only during terminal tissue
462 differentiation but not in cell-state transitions⁴⁶. Instead, we find pre-existing E-P contacts
463 important for the memory effect. Indeed, it is thought that pre-formed E-P contacts may prime
464 some genes for activation^{20,25,47–50}, but additional triggers are required for transcription to take
465 place. We speculate that excess H3K27ac activates enhancers, and those that are structurally
466 in a high contact probability with their promoter targets can maintain active transcription even
467 after the removal of ectopic acetylation.

468

469 Chromatin looping is commonly discussed in the context E-P contacts, or as the interplay
470 between CTCF and cohesin that gives rise to loop extrusion-driven interactions. Our study
471 highlights the importance and the potency of a third - often overlooked - type of focal contact
472 corresponding to repressive chromatin loops. Somewhat counterintuitively, we find that excess
473 chromatin activation and opening reinforces looping between loci marked by repressive
474 chromatin signatures. One such class of loops corresponds to Polycomb (PcG) contacts that
475 seem to be central to sustained gene expression downregulation. In neural progenitors PcG
476 loci are known to exhibit transcriptional memory in *cis*, and this memory is linked to antagonism
477 between Polycomb Repressive Complex 2 (PRC2) and activating signals⁵¹. Thus, one
478 possible explanation is that excess genome-wide chromatin activation dilutes activating
479 complexes away from PcG targets, tipping the balance towards gene downregulation.
480 Crucially, as continued gene downregulation involves minimal – if any – change in the
481 H3K27me3-H3K27ac balance at promoters, enhanced spatial sequestration of PcG loci
482 appears to be central to the mechanisms of repression, constituting an architecture-based
483 memory of a repressive state. Indeed, besides local chromatin compaction^{52,53}, long range
484 contacts are thought to be a mechanism by which PcG complexes confer silencing both in
485 *Drosophila* and in mammals^{48,54–58}, thus it is plausible that chromatin organisation would also
486 be a mechanism of PcG-driven epigenetic memory⁵⁹. We also detect prominent looping
487 between H3K9me3 marked loci as a potential mechanism of gene downregulation which,
488 contrarily to PcG loops, does not show memory. In the future it might be interesting to
489 investigate if H3K9me3 contacts are mediated by homotypic chromatin interactions, or if
490 looping involves the action of chromatin binding proteins such as HP1⁶⁰, perhaps with specific
491 associated partners that might gain interactions upon changes in chromatin acetylation state.
492

493 Other than fine-scale changes precisely linked to differences in gene expression, acute
494 disruption of the acetylation landscape led to important changes in global genome folding. The

495 increase in *trans* contacts points to the possibility that histone acetylation might be an
496 important determinant of intrachromosomal interactions as well as chromosome territories.
497 Indeed, it has been shown that long, highly transcribed genes or gene dense regions extend
498 from chromosome territories^{21,61–63}, although this has been attributed to binding of
499 ribonucleoproteins to nascent transcripts rather than to the acetylation state *per se*. Using
500 biophysical modelling we found that, by increasing the stiffness of the chromatin fibre²¹, we
501 can indeed accurately recapitulate the *trans* contact ratio observed in TSA. While the
502 determinants of *trans* contacts remain largely elusive, it is widely accepted that homotypic
503 interactions between domains of the same epigenetic state are the major driving force of
504 chromosome compartmentalisation⁶⁴. Thus, it was reasonable to anticipate that histone
505 hyperacetylation would have an impact on A and B compartments. However, to our surprise
506 global chromatin activation weakened rather than strengthened A-A compartment interactions
507 to an extent that is comparable to what occurs during ESC differentiation²⁰. Interestingly,
508 simulations that we carried out in an attempt to understand whether increased chromatin
509 stiffness can give rise to excess *trans* contacts efficiently predicted the change in compartment
510 interactions that we observed in the Micro-C data. This suggests that chromatin stiffness is an
511 important biophysical determinant of not just interchromosomal contacts but also A/B
512 compartmentalisation.

513

514 Finally, we found that these perturbed compartment interactions can partially persist beyond
515 the recovery period, signifying that 3D structures carry a partial memory of their past state.
516 This might be explained with hysteresis, the dependence of a system's behaviour on its history.
517 Hysteresis is an emerging principle in 3D genome organisation which was found to be critical
518 to model certain characteristics of genome folding, ranging from *cis* contacts in gene
519 expression control⁶⁵, to organisation of the interphase nucleus⁶⁶. Such a principle has been
520 demonstrated to exist by experimental approaches, whereby interphase chromosome
521 conformation was found to depend on the condensin complex that carried out mitotic
522 chromosome condensation in the previous cell cycle⁶⁷. Our study is in line with these
523 observations and provides empirical evidence of an architectural memory both at global scale
524 and at gene level. Biophysical modelling has shown that 3D genome folding might be a critical
525 element to stabilise epigenetic memory in interphase cells, providing further support to
526 association that we found between 3D genome folding and cellular memory^{68–70}. In the future
527 it will be critical to understand how mitotic events in the nucleus might be used by cells to
528 modulate or maintain their identity, as well as what molecular factors contribute to this process.

529

530

531 **References**

532

- 533 1. Schlesinger, S. & Meshorer, E. Open Chromatin, Epigenetic Plasticity, and Nuclear
534 Organization in Pluripotency. *Dev Cell* **48**, 135–150 (2019).
- 535 2. Pachano, T., Crispato, G. & Rada-Iglesias, A. Polycomb proteins as organizers of
536 3D genome architecture in embryonic stem cells. *Brief Funct Genomics* **18**, 358–
537 366 (2019).
- 538 3. Macrae, T. A., Fothergill-Robinson, J. & Ramalho-Santos, M. Regulation, functions
539 and transmission of bivalent chromatin during mammalian development. *Nat Rev
540 Mol Cell Biol* **24**, 6–26 (2023).
- 541 4. Urso, A. D. & Brickner, J. H. Mechanisms of epigenetic memory. (2014)
542 doi:10.1016/j.tig.2014.04.004.
- 543 5. Atlasi, Y. & Stunnenberg, H. G. The interplay of epigenetic marks during stem cell
544 differentiation and development. *Nat Rev Genet* **18**, 643–658 (2017).
- 545 6. Yoshida, M., Kijima, M., Akita, M. & Beppu, T. Potent and specific inhibition of
546 mammalian histone deacetylase both in vivo and in vitro by trichostatin A. *Journal
547 of Biological Chemistry* **265**, 17174–17179 (1990).
- 548 7. Willemin, A., Szabó, D. & Pombo, A. Epigenetic regulatory layers in the 3D
549 nucleus. *Mol Cell* **84**, 415–428 (2024).
- 550 8. Piunti, A. & Shilatifard, A. Epigenetic balance of gene expression by polycomb and
551 compass families. *Science* (1979) **352**, (2016).
- 552 9. Lagger, G. et al. Essential function of histone deacetylase 1 in proliferation control
553 and CDK inhibitor repression. *EMBO Journal* **21**, 2672–2681 (2002).
- 554 10. Dovey, O. M., Foster, C. T. & Cowley, S. M. Histone deacetylase 1 (HDAC1), but not
555 HDAC2, controls embryonic stem cell differentiation. *Proc Natl Acad Sci U S A*
556 **107**, 8242–8247 (2010).
- 557 11. Karantzali, E. et al. Histone deacetylase inhibition accelerates the early events of
558 stem cell differentiation: Transcriptomic and epigenetic analysis. *Genome Biol* **9**,
559 (2008).
- 560 12. Kidder, B. L. & Palmer, S. HDAC1 regulates pluripotency and lineage specific
561 transcriptional networks in embryonic and trophoblast stem cells. *Nucleic Acids
562 Res* **40**, 2925–2939 (2012).
- 563 13. Jamaladdin, S. et al. Histone deacetylase (HDAC) 1 and 2 are essential for
564 accurate cell division and the pluripotency of embryonic stem cells. *Proc Natl
565 Acad Sci U S A* **111**, 9840–9845 (2014).
- 566 14. Fejes Tóth, K. et al. Trichostatin A-induced histone acetylation causes
567 decondensation of interphase chromatin. *J Cell Sci* **117**, 4277–4287 (2004).
- 568 15. Otterstrom, J. et al. Super-resolution microscopy reveals how histone
569 tail acetylation affects DNA compaction within nucleosomes in vivo. *Nucleic
570 Acids Res* **47**, 8470–8484 (2019).
- 571 16. Szabo, Q. et al. Regulation of single-cell genome organization into TADs and
572 chromatin nanodomains. *Nat Genet* **52**, 1151–1157 (2020).
- 573 17. Hsieh, T.-H. S. et al. Resolving the 3D Landscape of Transcription-Linked
574 Mammalian Chromatin Folding. *Mol Cell* 1–15 (2020)
575 doi:10.1016/j.molcel.2020.03.002.

- 576 18. Hsieh, T. H. S. *et al.* Enhancer–promoter interactions and transcription are largely
577 maintained upon acute loss of CTCF, cohesin, WAPL or YY1. *Nat Genet* **54**, 1919–
578 1932 (2022).
- 579 19. Goel, V. Y., Huseyin, M. K. & Hansen, A. S. Region Capture Micro-C reveals
580 coalescence of enhancers and promoters into nested microcompartments. 1–8
581 (2022).
- 582 20. Bonev, B. *et al.* Multiscale 3D Genome Rewiring during Mouse Neural
583 Development. *Cell* **171**, 557–572.e24 (2017).
- 584 21. Leidescher, S. *et al.* Spatial organization of transcribed eukaryotic genes. *Nat Cell
585 Biol* **24**, 327–339 (2022).
- 586 22. Orsi, G. A. *et al.* Biophysical ordering transitions underlie genome 3D re-
587 organization during cricket spermiogenesis. *Nat Commun* **14**, 1–16 (2023).
- 588 23. Di Stefano, M. & Cavalli, G. Integrative studies of 3D genome organization and
589 chromatin structure. *Curr Opin Struct Biol* **77**, 102493 (2022).
- 590 24. Girard, M., De La Cruz, M. O., Marko, J. F. & Erbaş, A. Heterogeneous flexibility can
591 contribute to chromatin segregation in the cell nucleus. *Phys Rev E* **110**, 1–12
592 (2024).
- 593 25. Cruz-Molina, S. *et al.* PRC2 Facilitates the Regulatory Topology Required for
594 Poised Enhancer Function during Pluripotent Stem Cell Differentiation. *Cell Stem
595 Cell* **20**, 689–705.e9 (2017).
- 596 26. Crispatzu, G. *et al.* The chromatin, topological and regulatory properties of
597 pluripotency-associated poised enhancers are conserved in vivo. *Nat Commun*
598 **12**, 1–17 (2021).
- 599 27. Fraser, J. *et al.* Hierarchical folding and reorganization of chromosomes are linked
600 to transcriptional changes in cellular differentiation. *Mol Syst Biol* **11**, 1–14 (2015).
- 601 28. Winick-Ng, W. *et al.* Cell-type specialization is encoded by specific chromatin
602 topologies. *Nature* **599**, 684–691 (2021).
- 603 29. Yao, Y.-L., Yang, W.-M. & Seto, E. Regulation of Transcription Factor YY1 by
604 Acetylation and Deacetylation. *Mol Cell Biol* **21**, 5979–5991 (2001).
- 605 30. Faiola, F. *et al.* Dual Regulation of c-Myc by p300 via Acetylation-Dependent
606 Control of Myc Protein Turnover and Coactivation of Myc-Induced Transcription.
607 *Mol Cell Biol* **25**, 10220–10234 (2005).
- 608 31. Van Den Brink, S. C. *et al.* Symmetry breaking, germ layer specification and axial
609 organisation in aggregates of mouse embryonic stem cells. *Development
610 (Cambridge)* **141**, 4231–4242 (2014).
- 611 32. Beccari, L. *et al.* Multi-axial self-organization properties of mouse embryonic
612 stem cells into gastruloids. *Nature* **562**, 272–276 (2018).
- 613 33. Harris, H. L. *et al.* Chromatin alternates between A and B compartments at
614 kilobase scale for subgenic organization. *Nat Commun* **14**, (2023).
- 615 34. Argelaguet, R. *et al.* Multi-omics profiling of mouse gastrulation at single-cell
616 resolution. *Nature* **576**, 487–491 (2019).
- 617 35. Zhang, Y. *et al.* Dynamic epigenomic landscapes during early lineage
618 specification in mouse embryos. *Nat Genet* **50**, 96–105 (2018).
- 619 36. Xie, W. *et al.* Epigenomic analysis of multilineage differentiation of human
620 embryonic stem cells. *Cell* **153**, 1134–1148 (2013).
- 621 37. Gifford, C. A. *et al.* Transcriptional and epigenetic dynamics during specification
622 of human embryonic stem cells. *Cell* **153**, 1149–1163 (2013).

- 623 38. Creyghton, M. P. et al. Histone H3K27ac separates active from poised enhancers
624 and predicts developmental state. *Proc Natl Acad Sci U S A* **107**, 21931–21936
625 (2010).
- 626 39. Rada-Iglesias, A. et al. A unique chromatin signature uncovers early
627 developmental enhancers in humans. *Nature* **470**, 279–285 (2011).
- 628 40. Kim, H. S. et al. Pluripotency factors functionally premark cell-type-restricted
629 enhancers in ES cells. *Nature* **556**, 510–514 (2018).
- 630 41. Schick, S. et al. Acute BAF perturbation causes immediate changes in chromatin
631 accessibility. *Nat Genet* **53**, 269–278 (2021).
- 632 42. Iurlaro, M. et al. Mammalian SWI/SNF continuously restores local accessibility to
633 chromatin. *Nat Genet* **53**, 279–287 (2021).
- 634 43. Ghavi-Helm, Y. et al. Enhancer loops appear stable during development and are
635 associated with paused polymerase. *Nature* **512**, 96–100 (2014).
- 636 44. Benabdallah, N. S. et al. Decreased Enhancer-Promoter Proximity Accompanying
637 Enhancer Activation. *Mol Cell* **76**, 473-484.e7 (2019).
- 638 45. Ing-Simmons, E. et al. Independence of chromatin conformation and gene
639 regulation during Drosophila dorsoventral patterning. *Nat Genet* **53**, 487–499
640 (2021).
- 641 46. Pollex, T. et al. Enhancer–promoter interactions become more instructive in the
642 transition from cell-fate specification to tissue differentiation. *Nat Genet* **56**, 686–
643 696 (2024).
- 644 47. Jin, F. et al. A high-resolution map of the three-dimensional chromatin
645 interactome in human cells. *Nature* **503**, 290–294 (2013).
- 646 48. Schoenfelder, S. et al. Polycomb repressive complex PRC1 spatially constrains
647 the mouse embryonic stem cell genome. *Nat Genet* **47**, 1179–1186 (2015).
- 648 49. Stadhouders, R. et al. Transcription factors orchestrate dynamic interplay
649 between genome topology and gene regulation during cell reprogramming. *Nat
650 Genet* **50**, 238–249 (2018).
- 651 50. Paliou, C. et al. Preformed chromatin topology assists transcriptional robustness
652 of Shh during limb development. *Proc Natl Acad Sci U S A* **116**, 12390–12399
653 (2019).
- 654 51. Holoch, D. et al. *A Cis-Acting Mechanism Mediates Transcriptional Memory at
655 Polycomb Target Genes in Mammals*. *Nature Genetics* vol. 53 (Springer US, 2021).
- 656 52. Margueron, R. et al. Ezh1 and Ezh2 Maintain Repressive Chromatin through
657 Different Mechanisms. *Mol Cell* **32**, 503–518 (2008).
- 658 53. Lau, M. S. et al. Mutation of a nucleosome compaction region disrupts Polycomb-
659 mediated axial patterning. *Science (1979)* **355**, 1081–1084 (2017).
- 660 54. Lanzuolo, C., Roure, V., Dekker, J., Bantignies, F. & Orlando, V. Polycomb response
661 elements mediate the formation of chromosome higher-order structures in the
662 bithorax complex. *Nat Cell Biol* **9**, 1167–1174 (2007).
- 663 55. Bantignies, F. et al. Polycomb-dependent regulatory contacts between distant
664 hox loci in drosophila. *Cell* **144**, 214–226 (2011).
- 665 56. Cheutin, T. & Cavalli, G. Loss of PRC1 induces higher-order opening of Hox loci
666 independently of transcription during Drosophila embryogenesis. *Nat Commun* **9**,
667 1–11 (2018).

- 668 57. Ogiyama, Y., Schuettengruber, B., Papadopoulos, G. L., Chang, J. M. & Cavalli, G.
669 Polycomb-Dependent Chromatin Looping Contributes to Gene Silencing during
670 Drosophila Development. *Mol Cell* **71**, 73–88.e5 (2018).
- 671 58. Mas, G. et al. Promoter bivalency favors an open chromatin architecture in
672 embryonic stem cells. *Nat Genet* **50**, 1452–1462 (2018).
- 673 59. Murphy, S. E. & Boettiger, A. N. Polycomb repression of Hox genes involves spatial
674 feedback but not domain compaction or phase transition. *Nat Genet* **56**, 493–504
675 (2024).
- 676 60. Bártová, E. et al. Nuclear levels and patterns of histone H3 modification and HP1
677 proteins after inhibition of histone deacetylases. *J Cell Sci* **118**, 5035–5046
678 (2005).
- 679 61. Mahy, N. L., Perry, P. E. & Bickmore, W. A. Gene density and transcription
680 influence the localization of chromatin outside of chromosome territories
681 detectable by FISH. *Journal of Cell Biology* **159**, 753–763 (2002).
- 682 62. Chambeyron, S., Da Silva, N. R., Lawson, K. A. & Bickmore, W. A. Nuclear re-
683 organisation of the Hoxb complex during mouse embryonic development.
684 *Development* **132**, 2215–2223 (2005).
- 685 63. Brown, J. M. et al. Association between active genes occurs at nuclear speckles
686 and is modulated by chromatin environment. *Journal of Cell Biology* **182**, 1083–
687 1097 (2008).
- 688 64. Hildebrand, E. M. & Dekker, J. Mechanisms and Functions of Chromosome
689 Compartmentalization. *Trends Biochem Sci* **45**, 385–396 (2020).
- 690 65. Xiao, J., Hafner, A. & Boettiger, A. N. How subtle changes in 3d structure can
691 create large changes in transcription. *Elife* **10**, 1–27 (2021).
- 692 66. Di Stefano, M., Nützmann, H. W., Marti-Renom, M. A. & Jost, D. Polymer
693 modelling unveils the roles of heterochromatin and nucleolar organizing regions
694 in shaping 3D genome organization in *Arabidopsis thaliana*. *Nucleic Acids Res* **49**,
695 1840–1858 (2021).
- 696 67. Hoencamp, C. et al. 3D genomics across the tree of life reveals condensin II as a
697 determinant of architecture type. *Science (1979)* **372**, 984–989 (2021).
- 698 68. Owen, J. A., Osmanović, D. & Mirny, L. Design principles of 3D epigenetic memory
699 systems. *Science (1979)* **382**, (2023).
- 700 69. Jost, D. & Vaillant, C. Epigenomics in 3D: Importance of long-range spreading and
701 specific interactions in epigenomic maintenance. *Nucleic Acids Res* **46**, 2252–
702 2264 (2018).
- 703 70. Michieletto, D., Orlandini, E. & Marenduzzo, D. Polymer model with epigenetic
704 recoloring reveals a pathway for the de novo establishment and 3D organization
705 of chromatin domains. *Phys Rev X* **6**, 1–15 (2016).
- 706

707 **Material and Methods**

708 **EXPERIMENTAL METHOD DETAILS**

709 **Embryonic stem cell culture**

710 E14GT2a p14 cells were purchased from MMRRC, UC Davis, CTCF-GFP-AID cells were gift
711 from R. Saldana-Meyer. ESCs were cultured on plastic plates coated with 0.1% gelatin
712 (Sigma-Aldrich #G1890-100G) in serum-LIF medium (GMEM (Gibco #2171002), with 15%
713 FBS (ThermoFisher #26140079 USA origin), 1x Glutamax (ThermoFisher #35050038), 1x
714 MEM Non-Essential Amino Acids (ThermoFisher #11140035), 50 U Penicillin-Streptomycin
715 (Gibco #15140122), 0.1 mM Sodium Pyruvate (Gibco #11360070), 0.1 mM 2-Mercaptoethanol
716 (Gibco #31350010), and 1,000 U/ml LIF (Sigma-Aldrich #ESG1107)). Cells were passaged
717 every 2-3 days using TrypLE Express Enzyme (Gibco #12604013). Cell lines were regularly
718 tested for mycoplasma infection. Cell viability was assessed by staining with Trypan Blue
719 (Gibco # 15250061) and cells were counted on a Countess 3 automated cell counter
720 (Invitrogen). HDAC inhibition was performed by treating cells with 100 ng/ml Trichostatin A
721 (Sigma-Aldrich #647925) for 4 hours. Control cells were treated with 0.01% DMSO for the
722 same duration. For recovery, cells were washed once with PBS and were incubated with fresh
723 mESC media for 10 minutes. This PBS wash/media change was repeated 2 more times before
724 incubating cell for a total of 24 hours.

725

726 **Gastruloid culture**

727 Gastruloids for RNA-seq and immunostaining experiments were generated as described in⁷¹.
728 Briefly, CTCF-GFP-AID cells were harvested, centrifuged and washed twice with PBS.
729 Following, cells were resuspended in N2B27 medium and counted. 300 cells were seeded in
730 each well of a round-bottomed, low-attachment 96-well plate (Greiner #650970) in N2B27
731 medium. After 48 hours, a 24-hour pulse of 3 µM Chiron was administered and media was
732 changed every day. HDAC inhibition was carried out by treating gastruloids with 20 ng/ml ml
733 Trichostatin A (Sigma-Aldrich #647925) for 4 hours immediately prior to the Chiron pulse (44-
734 48 hours). TSA was removed from the medium by changing N2B27 media three times with 10
735 minutes of incubation in between. Control cells were washed similarly.

736

737 **Western blotting**

738 For western blotting ~10⁷ mESCs were dissociated, washed once in PBS, resuspended in 200
739 µl of Cell Lysis Buffer (85mM KCl; 0.5% NP40; 5mM HEPES pH. 8; 1X EDTA-free Protease
740 inhibitor (Roche); 5mM sodium butyrate) and incubated on ice for 15 minutes. Afterwards, cell
741 nuclei were pelleted at 2000g for 5 minutes at 4°C. The supernatant (cytoplasmic fraction) was

742 separated, and nuclei were resuspended in 100 μ l RIPA buffer (50 mM Tris pH 7.5; 150 mM
743 NaCl; 1% NP40; 0.5 % NaDoc; 0.1% SDS; 1X EDTA-free Protease inhibitor (Roche
744 #04693132001); 5mM sodium butyrate). Following a 10-minute incubation on ice, chromatin
745 was digested for 15 min at 37°C with 0.0125 U/ μ l MNase and 1mM of CaCl₂. Extracts were
746 cleared by 30 minutes of centrifugation at 14000 rpm at 4°C. Protein yield was quantified using
747 Pierce BCA protein assay kit (ThermoFisher #A65453). Samples were mixed with 4x NuPage
748 LDS sample buffer (ThermoFisher #NP0007) and boiled for 10 minutes at 95°C. 2 μ g denatured
749 protein extract was loaded per lane on a NuPAGE™ 4 -12 %, Bis-Tris gel (ThermoFisher
750 #NP0321BOX). Transfer onto nitrocellulose membranes was performed using the Trans-Blot
751 Turbo Transfer System (Biorad). Membranes were stained with Ponceau S for 5 minutes, then
752 blocked for at least 30 min with 3% BSA in PBS + 0.1% Triton-X100 prior to incubation with
753 primary antibody overnight at 4°C with the following dilutions: α -H3K27ac 1:7500 (Active Motif
754 #39133); α -pan-acetyl lysine 1:1000 (ThermoFisher, #66289-1-IG); α -lamin B1 1:10000
755 (abcam #ab16048); α -Vinculin 1:1000 (Santa Cruz Biotechnology #sc-73614). Membranes
756 were washed three times >5 minutes in PBS +0.1% Tween-20 and were incubated with
757 secondary antibodies (α -Rabbit IgG-Peroxidase antibody (Sigma-Aldrich #A0545) or α -Mouse
758 IgG-Peroxidase antibody (Sigma-Aldrich #A9044)) at 1:16000 dilution for 1 hour at room
759 temperature. After three >5-minute washes with PBS-0.1% Tween-20 at room temperature,
760 membranes were developed using the SuperSignal West Dura Extended Duration Substrate
761 solution (ThermoFisher #34075) for 1 minute and imaged with a Bio-Rad ChemiDoc imager.
762

763 **Flow Cytometry**

764 1-3x10⁶ mESCs were dissociated with TrypLE, pelleted, and resuspended in PBS. For cell
765 cycle analysis, dissociated mESCs were washed once in PBS and pelleted and fixed in cold
766 70% ethanol for 30 min at 4°C. Cells were stained with the Propidium Iodide Flow Cytometry
767 Kit (Abcam #ab139418) according to manufacturer's instruction. Flow cytometry was
768 performed on a Miltenyi MACSQuant instrument, and analysis was performed using the
769 FlowJo software.
770

771 **Gastruloid immunostaining**

772 Gastruloid immunostaining protocol was adopted from⁷². Plastic material was pre-coated with
773 the blocking solution (PBS + 10% FBS + 0.2% Triton-X100). Using a cut P1000 tip, gastruloids
774 were collected into 15 mL centrifuge tubes. Following a PBS wash, gastruloids were
775 transferred to with 2mL 4% PFA in 6-well plates and were fixed overnight at 4°C. For washes,
776 gastruloids were transferred serially across three PBS-filled wells and were incubated for 10
777 minutes in the last one. Gastruloids were blocked in PBS+FT (PBS + 10% FBS + 0.2% Triton-
778 X100) for 1 hour at room temperature, then incubated with primary antibodies (α -Brachyury

779 1:500 (Santa Cruz Biotechnologies #sc-166962), α -Sox2 1:500 (eBioscience #15208187), α -
780 H3K27ac 1:200 (Active Motif #39133)) in PBS+FT and 1 ug/ml DAPI overnight at 4°C with
781 orbital shaking. Gastruloids were washed by sequentially transferring them in 3 wells filled with
782 PBS+FT and incubating them for 20 minutes in the last one. Staining with secondary antibody
783 (α -Rabbit Alexa Fluor Plus 488 1:400 (ThermoFisher #A32731); α -Rabbit Alexa Fluor Plus 555
784 1:400 (ThermoFisher #A32794); α -Rat Alexa Fluor Plus 647 1:400 (ThermoFisher #A48265)),
785 and 1 ug/ml DAPI, as well as washes were carried out similarly to primary antibody.
786 Gastruloids were mounted in ~30uL of Fluoromount-G (ThermoFisher #00-4958-02) and were
787 kept at 4 °C before imaging.

788

789 **Image acquisition and quantification**

790 Confocal imaging was performed using a Confocal Zeiss LSM980 Airyscan II equipped with a
791 20x objective. Diodes laser 405, 488, 561 and 639 nm were used for fluorophore excitations,
792 leading to blue, green, red and far-red channels. For each gastruloid 3 z-stacks were taken
793 and using the Fiji software, maximum intensities were projected to manually define areas of
794 H3K27ac, Sox2 and Brachyury expression as well as DAPI staining.

795

796 **RNA isolation for RNA-seq**

797 RNA was isolated using the RNeasy mini kit (Qiagen 74104). Cells were detached with
798 TrypLE, lysed in RLT buffer with β -mercaptoethanol and lysates were processed according to
799 manufacturer's instruction. For mESCs columns and buffers supplied with the RNeasy kit were
800 used, while for gastruloids the Zymo RNA Clean & Concentrator-5 (Zymo Research #R1015)
801 reagents were used. On-column DNase-I digestion (Qiagen #79254) was performed as
802 recommended. RNA samples were sent to BGI Tech Solutions (Hongkong) for strand-specific
803 transcriptome sequencing. Samples were sequenced at a depth of 50 million 150 bp paired
804 end reads. All experiments were performed in triplicates.

805

806 **Micro-C library preparation and sequencing**

807 Micro-C libraries were generated with the Dovetail™ Micro-C Kit protocol v1.0 with minor
808 modifications. Briefly, 10^6 mESC were washed with PBS and were frozen at -80°C for at least
809 1 hour. Cell pellets were thawed and crosslinked first with 3 mM DSG (ThermoFisher
810 #A35392) in PBS for 10 minutes at RT with rotation, then formaldehyde was added at 1% final
811 concentration for further 10 minutes. The pellets were washed twice with PBS and digested
812 with MNase according to kit instructions. MNase digestion was routinely verified by
813 decrosslinking a small amount of chromatin and assessing fragment distribution on a
814 Bioanalyzer 2100 instrument (Agilent). If the digestion profile showed 60% - 70%
815 mononucleosomal DNA fraction, on-bead proximity ligation was performed, followed by

816 reversed cross-linking and DNA purification. End repair and adapter ligation were performed
817 using the NEBNext Ultra II DNA Library Prep Kit for Illumina (NEB #E7645). Following, DNA
818 was purified using SPRI beads (Beckman #B23318) as described in the Micro-C user manual.
819 Finally, biotin pulldown and library amplification were performed according to Dovetail Micro-
820 C Kit User Guide and using Dovetail Micro-C Kit reagents, only replacing the Dovetail Primers
821 (Universal and Index) with NEBNext primers. Libraries were pooled and sent to BGI Tech
822 Solutions (Hongkong) for 100-bp paired-end sequencing to obtain roughly 2-3 billion reads for
823 each replicate in the present study.

824

825 **Chromatin Immunoprecipitation followed by sequencing (ChIP-seq)**

826 Chromatin immunoprecipitation was performed as described previously⁷³. Cells were collected
827 with TrypLE (ThermFisher #12604013) and fixed with 1% methanol-free formaldehyde in
828 mESC media for 10 minutes with rotation at RT. Glycine (2.5M Glycine in PBS) was used to
829 stop the fixation for 10 minutes with rotation at RT. Fixed cells were centrifuged at 500 g for 5
830 minutes at 4°C, washed twice in 1x ice-cold PBS and snap frozen in liquid nitrogen until further
831 use. Following thawing, cells were spiked-in with 8% HEK-293 cells and chromatin extraction
832 was performed as in⁷⁴. 15 µg of chromatin was used for each replicate of histone ChIP, and
833 50 µg for CTCF and YY1 ChIP, with 6–8 µg of antibody. Since the above protocol was not
834 suitable for YY1, we followed the protocol described by⁷⁵. Briefly, fixed cells resuspended in
835 SDS buffer, followed by sonication and preparation for immunoprecipitation in a homemade
836 buffer. Next, the mixture was incubated overnight at 4°C with Protein G beads (Invitrogen
837 #10004D), washed with both low and high-salt buffers, reverse-crosslinked in an elution buffer,
838 and purified using a QIAQuick PCR purification kit (Qiagen # 28104). Antibodies used in this
839 study were: H3K4me1 Active Motif #39297), H3K4me3 (Milipore #04-745), H3K27ac (Active
840 Motif #39133), H3K9me3 (abcam ab8898), H3K27me3 (Active Motif #39155), H2AK119Ub
841 (Cell Signalling #8240S), CTCF (Active Motif #61311), and YY1 (abcam 109237). Sequencing
842 libraries were constructed using NEBNext Ultra II DNA Library Prep Kit for Illumina (NEB
843 #E7645), pooled and sent to BGI Tech Solutions (Hongkong) for 100-bp paired-end
844 sequencing to obtain roughly 30-50 million reads for each replicate. All experiments were
845 performed in duplicates.

846

847 **Assay for transposase accessible chromatin (ATAC-seq)**

848 For each replicate, 9x10⁴ mESCs were collected with TrypLE (ThermFisher # 12604013) and
849 were mixed with 10⁴ HEK-293 cells. Samples were processed using the Active Motif ATAC-
850 seq kit (Active Motif #53150) following manufacturer's instructions without modifications.
851 ATAC-seq libraries were pooled and sent to BGI Tech Solutions (Hongkong) for 100-bp paired-

852 end sequencing to obtain roughly 30-50 million reads for each replicate. All experiments were
853 performed in duplicates.

854 QUANTIFICATION AND STATISTICAL ANALYSES

855 RNA-seq analysis

856 RNA-seq samples were mapped using the *align* function of the Subread package (2.0.6).
857 Subread command *featureCounts* (with options “-p --countReadPairs -s 2 -t exon”) and the
858 feature file UCSC RefSeq GTF file for mm10 were used to generate count tables that were
859 then used as an input for the DEseq2⁷⁶ to perform the differential analysis (Supplementary
860 Table 2). Gene Ontology analysis was performed significantly up- and down-regulated genes
861 (p-adjust ≤ 0.05, |log2FC| ≤ 1) using the *enrichGO* function from the clusterProfiler package⁷⁷
862 (Supplementary Table 3). Volcano plots and scatter plots were produced in R using the
863 EnhancedVolcano and ggplot2 libraries respectively.

864

865 ChIP-seq and ATAC-seq analysis

866 ChIP-seq and ATAC-seq samples were mapped using bowtie2 v.2.4.4⁷⁸ with command
867 “*bowtie2 -p 12 --no-mixed --no-discordant*” against the mm10 and hg19 genomes. Then,
868 samtools v.1.9⁷⁹ was used to filter out low-quality reads (command “*samtools view -b -q 30*“)
869 and Sambamba v1.0⁸⁰ was used to sort (command “*sambamba sort*”), deduplicate and index
870 bam files (“*sambamba markdup --remove-duplicates*”) with default parameters. Following,
871 samtools was used to count both human a mouse reads (command “*samtools view -c*“) to
872 calculate down-sampling factor (dF) for spike-in normalisation as described in⁸¹. Next, bam
873 files were downscaled accordingly using samtools (command “*samtools view -b -s dF*“) and
874 bigwig files were produced using the deepTools package⁸² with command “*bamCoverage --*
875 *normalizeUsing none --ignoreDuplicates -e 0 -bs 10*“. Finally, ChIP-seq tracks in were
876 visualized using the IGV v.2.16.1 software⁸³ or HiGlass⁸⁴. ATAC-seq and ChIP-seq peaks were
877 called on each replicate using MACS3 with a q value cutoff 0.05, and for histone marks with
878 the additional parameters *--broad --broad-cutoff 0.1s*⁸⁵. Finally, peaks detected from both
879 replicates were filtered and all downstream analyses were carried out using this consensus
880 peak set. For differential peak calling the diffBind⁸⁶ R package was used with normalisation
881 “*normalize=DBA_NORM_LIB, spikein = TRUE*“, analysis method “*method=DBA_DESEQ2*“,
882 and FDR < 0.05 cutoff. Heatmaps and metaplots were produced using the *computeMatrix*
883 function of the deepTools package, and plotted using the *plotHeatmap* and *plotProfile*
884 functions. ChIP-seq bloxplots were also created by deepTools using the the
885 *multiBigwigSummary* function and were plotted by ggplot2 in R. Chromosome wide H3K27ac

886 read density plots were generated using a custom R script published in⁸¹. ChIP-seq peak
887 distribution and annotation were carried out with ChIPseeker's⁸⁷ *plotPeakProf* and
888 *annotatePeak* functions, respectively. Gene ontology analysis of annotated ChIP-seq peaks
889 was performed using the *enrichGO* function from the clusterProfiler package⁷⁷ (Supplementary
890 Table 3). For cumulative histograms, enhancer distance from TSSs was calculated using
891 bedtools closest function and was plotted by ggplot2 in R. Expression-matched control gene
892 set was derived using code from the AdelmanLab github repository
893 (<https://github.com/AdelmanLab/Expression-Matching>). Myc ChIP-seq dataset was published
894 in⁸⁸ and was downloaded from the GEO repository GSE90895.

895

896 Micro-C data analysis

897 **Generation of contact matrices and standard analyses.** Micro-C data was mapped using
898 the HiC-Pro v3.1.0 pipeline⁸⁹. Fastq reads were trimmed to 50 bp using TrimGalore (--
899 hardtrim5 50) (<https://github.com/FelixKrueger/TrimGalore>) and aligned to the mm10 (UCSC
900 Mouse GRCm38/mm10) reference genome using bowtie2⁷⁸ v2.4.4 (“--very-sensitive --L 30 --
901 score-min L, -0.6, -0.2 --end-to-end --reorder”), removing singleton, multi-hit and duplicated
902 reads. Minimum *cis* distance was set at 200 bp and non-informative pairs were removed. The
903 total numbers of valid read-pairs per sample are reported in Supplementary Table 1. Contact
904 matrices in the .cool file format were generated using cooler⁹⁰ v.0.10.2 at 100 bp resolution
905 (command “*cooler cload pairs -c1 2 -p1 3 -c2 5 -p2 6 ./scripts/chrom_sizes.txt:100*”).
906 Similarities between replicates (5 replicates for DMSO and TSA; 2 replicates for 24-hour
907 recovery) were measured using the Stratum-adjusted Correlation Coefficient (SCC) applying
908 *HiCRep* v1.12. (<https://github.com/TaoYang-dev/hicrep>)⁹¹ on chromosomes 2, 9, 13, and 19
909 using the *get.scc* function with parameters resol=20kb and (lbr,ubr,h)=((0, 100kb,1), (100kb,
910 500kb,1), (500kb, 2Mb,2), (2Mb, 10Mb,4)). H values were previously trained using the *htrain()*
911 on two replicates (E and F) of the DMSO condition. Using 1.0-SCC, as a measure of the
912 similarity (0 - similar and 1 dissimilar) between replicates and hierarchical clustering analysis
913 using *hclust()* function in R with Ward.D2 method on the chromosome-averaged similarities,
914 allowed us to distinguish and group together the replicates of the different conditions,
915 motivating us to merge the valid-pairs of different replicates in a unique dataset for each
916 condition. Multiresolution .mcool files were obtained and normalized via the Iterative
917 Correction and Eigenvector decomposition algorithm (ICE) with default parameters (command
918 “*cooler zoomify -r 100, 400, 600, 800, 1000, 2000, 4000, 8000, 10000, 20000, 50000, 100000,*
919 *1000000, 10000000 file.cool -o file.mcool --balance*”)⁹² and were uploaded onto a local
920 HiGlass server for visualization⁸⁴. For comparison of architectural features between different
921 conditions contact maps were matched to contain approximately the same number of *cis*

922 contacts (Supplementary Table 1). All genomic snapshots of Micro-C maps were generated
923 using HiGlass v.1.11.7. Standard analyses (P-value curves, eigenvector analyses, saddle
924 plots, insulation score analysis) were performed using the cooltools (version 0.5.4) package.
925 **Loop analyses.** Loops were called using mustache v1.0⁹³ with default parameters (“--
926 *pThreshold* 0.1 —*sparsityThreshold* 0.88 —*octaves* 2”) on ICE-balanced maps at 1 kb and 4
927 kb resolutions. Redundant loops between different resolutions were filtered in 20 kb windows,
928 and in case of overlap loop coordinates were retained at the finer resolution. All aggregate
929 plots were created with the coolpuppy v1.1.0 package⁹⁴ and were normalised using expected
930 maps generated by cooltools. For differential looping, contacts that overlapped with the
931 corresponding loop anchor bin were summed for each loop and were summarized into a count
932 table: genome-wide count tables were created for each replicate at each resolution (command
933 “cooler dump --join -t pixels”) then filtered against loop using bedtools ‘pairtopair’ function⁹⁵.
934 The count tables from different conditions were used for differential analysis with DESeq2
935 (Supplementary Table 2). The thresholds p.adj < 0.05, |log2FoldChange| > 0.5 and baseMean
936 >= 10 were used to filter for significant changes in looping between conditions. Volcano plots
937 were produced in R using the EnhancedVolcano library. Loop subclasses were defined based
938 on the presence of ChIP-seq peaks at loop anchors (repressive: overlapping with H3K9me3,
939 H3K27me3 or H2AK119Ub peak; active: overlapping with H3K4me1, H3K4me3 or H3K27ac
940 peak; *de novo* H3K9me3 loops: loops only present in TSA overlapping with H3K9me3 peak;
941 CTCF: loop anchors within +/- 1kb of CTCF peaks; non-CTCF: no CTCF peak within +/- 2.5
942 kb of loop anchor) or presence of TSSs within 2 kb of either loop anchor. Enhancer-promoter
943 contacts for recovery vs non-recovery genes were taken from²⁰. Loop quantification boxplots
944 represent the observed/expected value of the central 5x5 pixels of aggregate plots that was
945 extracted from coolpuppy matrices using an in-house Python script. Loop anchors were
946 annotated using the *annotatePeak* function of the ChIPseeker R package, and annotated
947 anchors within <10 kb from TSSs were used for GO enrichment with the *enrichGO* function of
948 clusterProfiler library (Supplementary Table 3).

949

950 **Biophysical modelling**

951 Two polymeric systems were prepared in 30 and 5 replicates respectively with 1 and 20 chains
952 of 20 mega-basepairs (Mbp) each. Each chain-bead was of unitary mass ($m = 1.0$), hosting
953 $\nu = 5$ kilo-base pairs (kbp) of DNA sequence and has a diameter of σ . This representation
954 was obtained with the Kremer-Grest bead-spring model⁹⁶ with the same parameter as in⁹⁷.

$$955 \quad H = U_{EV} + U_C + U_{BEND}(1)$$

956 The first term was a truncated and shifted Lennard-Jones potential that controls the *cis*- and
957 *trans*-chromosome excluded volume interactions:

958
$$U_{EV}(i,j) = \begin{cases} 4k_B T \epsilon_{ij} \left[\left(\frac{\sigma}{d_{i,j}} \right)^{12} - \left(\frac{\sigma}{d_{i,j}} \right)^6 + 1/4 \right] & \text{if } d_{i,j} \leq 2^{1/6}\sigma, \\ 0 & \text{if } d_{i,j} > 2^{1/6}\sigma. \end{cases} \quad (2)$$

959

960 where k_B is the Boltzmann constant, T the temperature, ϵ_{ij} is equal to 10 if $|i - j| = 1$, and 1
961 otherwise, σ was the thickness of the chain and $d_{i,j}$ is the modulus of $\vec{d}_{ij} = \vec{r}_i - \vec{r}_j$, that is the
962 distance vector between the monomers i and j at positions \vec{r}_i and \vec{r}_j , respectively.
963 The second term was a FENE potential that maintains chain connectivity between consecutive
964 beads on the same polymer chain:

965
$$U_C(i, i+1) = -0.5 K R_0^2 \ln \left[1 - \left(\frac{d_{i,i+1}}{R_0} \right)^2 \right] \quad (3)$$

966 where $K=0.33 k_B T / \text{nm}^2$ and $R_0=1.5\sigma$. The combined action of the connectivity and excluded
967 volume interaction between consecutive beads was such that the average bond length was
968 close to σ and never exceeded 1.1σ .

969 The third term is a (Kratky-Porod) bending potential:

970
$$U_{BEND} = \frac{k_B T K_\theta}{\sigma} \left(1 - \frac{d_{i,i+1} \cdot d_{i+1,i+2} \cdot d_{i+2,i}}{d_{i,i+1} d_{i+1,i+2} d_{i+2,i}} \right) \quad (4)$$

971 where K_θ is the chain persistence length.

972 The dynamics of the polymer model was simulated using the LAMMPS simulation package
973 (version 29 Oct 2020) integrating the (underdamped) Langevin equation of motion⁹⁸:

974
$$m \ddot{r}_{i\alpha} = -\partial_{i\alpha} H - \gamma \dot{r}_{i\alpha} + \eta_{i\alpha}(t) \quad (5)$$

975 where m is the mass of the bead that was set equal to the LAMMPS default value, H is the
976 Hamiltonian of the system in Eq. (1), the index i runs over all the particles in the system, and
977 $\alpha = (x, y, z)$ indicates the Cartesian components, and $\gamma = 0.5 \tau_{\text{LJ}}^{-1}$ is the friction coefficient with
978 $\tau_{\text{LJ}} = \sigma(m/\epsilon)^{1/2}$ is the Lennard-Jones time. The stochastic term $\eta_{i\alpha}$ satisfies the fluctuation-
979 dissipation conditions. The integration time step used in the numerical integration was equal
980 to $\Delta t = \alpha \tau_{\text{LJ}}$, where the factor α was adapted, as specified below, to the different stages of the
981 preparation and production runs.

982 **Preparation of the initial conformations.** Each chain is initially organized in a rod-like folding
983 featuring rosettes along the main axis and placed in random positions inside a confining
984 sphere of radius R^* so to set up the volume density of the system to 3% ($R^* = 25.5\sigma$ for the 1-
985 chain system and $R^* = 69.3\sigma$ for the 20-chain system), avoiding clashes with other chains. The
986 confining sphere is completely contained in a cubic simulation box with fixed boundary
987 conditions. After an energy minimization (*LAMMPS command*: minimize 1.0e-4 1.0e-6 100000
988 100000), each of the polymeric system is compressed to reach the DNA density of 10%. These
989 conditions were achieved by minimization (*LAMMPS command*: minimize 1.0e-4 1.0e-6
990 100000 100000) followed by molecular dynamics simulations of 600 τ_{LJ} (100,000 Δt with $\Delta t =$

991 0.006 τ_{LJ}) during which the radius of confining spheres is reduced from the minimum radius to
992 include all the particles of the chains at time 0 to the target radius R ($R = 17.1\sigma$ for the 1-chain
993 system and $R = 46.4\sigma$ for the 20-chain system). At the target volume density of 10%, the
994 polymer chains have parameters $\sigma \sim 54.2\text{nm}$ and $K_\theta \sim 92.3\text{nm}$. These estimates were done by
995 considering a fine-scale chromatin model with $\nu_{FS} = 100 \text{ bp}$, $\sigma_{FS} = 20 \text{ nm}$ and $K_{\theta FS} = 50 \text{ nm}$
996 and the coarse-grain procedure in⁹⁹. Finally, each polymeric system is relaxed with molecular
997 dynamics run of 30,600 τ_{LJ} (5,100,000 Δt with $\Delta t = 0.006 \tau_{\text{LJ}}$). By comparing the average
998 monomer Mean-Squared Displacement (MSD) in these relaxation runs and the MSD of non-
999 transcribed genes measured¹⁰⁰ by live-cell imaging, we obtained an approximated estimate of
1000 the simulated time (in τ_{LJ}) corresponding to 1s $\sim 9 \tau_{\text{LJ}}$. These conformations are next used as
1001 the initial conformations for the downstream simulations.

1002
1003 **A/B compartmentalisation.** To model the A/B compartmentalisation in the DMSO condition
1004 short-range interactions were used to test the attractions between the model regions which
1005 correspond to A/B compartments. As shown in Fig. 2d, the first and the last 1 Mb were
1006 assigned to telomeric region and 6 blocks of A/B domains each of 1.5 Mb were defined in the
1007 central part. These interactions have been modelled using attractive Lennard-Jones potentials
1008 (see **Equation 2**) with cutoff=2.5 σ , that allowed to include the attractive part of the Lennard-
1009 Jones potential. To allow efficient parameter sampling, we performed 4h simulations
1010 (21,600,000 Δt with $\Delta t = 0.006 \tau_{\text{LJ}}$) for just one chain by varying the strengths of compartments'
1011 interactions (E_{AA} and E_{BB}) were varied in the range 0.00-0.40 $k_B T$ in the 1-chain system with
1012 4h trajectories (21,600,000 Δt with $\Delta t = 0.006 \tau_{\text{LJ}}$). To infer these energies, A/B compartment-
1013 strengths at 10kb from the micro-C maps were matched against the correspondent quantities
1014 computed on the model chains⁶⁶. The compartment strength (CS) profile is obtained by
1015 partitioning the A- (B-) domains in 150 bins and by averaging within each of them the CS per
1016 10kb-bin of the Micro-C or models' contact-maps. The distance-cutoff for detecting contacts in
1017 the models was set to 150 nm~3beads. The Euclidean distance between A and B profiles was
1018 used to define compartment-specific ranks r_A and r_B ranging from 1 to max(r) where 1 is the
1019 best match with the experiments. A unique rank r was defined from the average of r_A and r_B .
1020 Finally, the similarity score was defined as $(r-\text{max}(r))/(\text{min}(r)-\text{max}(r))$ and it is equal to 1 for the
1021 condition that best describes the experimental CS-profile and to 0 for the least accurate one.
1022 This procedure resulted in the optimal values $E_{AA}=0.080$ and $E_{BB}=0.00$. Next, the DMSO and
1023 TSA condition were modelled by the system made of 20 chains simulated for with 4h-
1024 trajectories (21,600,000 Δt with $\Delta t = 0.006 \tau_{\text{LJ}}$). The optimized A/B-compartment attractions
1025 ($\epsilon_{AA}=0.080$ and $\epsilon_{BB}=0.00$) were maintained and the bending rigidity of the A- and B-
1026 compartment domains were differentially increased. We explored several combinations

1027 varying $K_{\theta A}$ between 1 and 16 times and $K_{\theta B}$ between 0 and 5 times the nominal persistence
1028 length of $K_\theta \sim 92.3\text{nm}$. The chromosome-averaged *trans*-contact ratios (TR) were computed
1029 by averaging the trans-contact ratio of 10kb-bins in each chromosome. The median was
1030 obtained on the distribution of these chromosome-averaged values. The absolute difference
1031 between the median values TR for all, only A and only B domains in the micro-C datasets and
1032 the models was used to define three ranks per each parameter set. A similarity score was
1033 defined from these three ranks applying a strategy analogous to one described above for CS
1034 profiles. Optimal values were $(K_{\theta A}, K_{\theta B}) = (1,0)K_\theta$ in DMSO and $(K_{\theta A}, K_{\theta B}) = (14,3)K_\theta$ in
1035 TSA. Model snapshots in Extended Data Fig. 2j were prepared using VMD¹⁰¹.

1036

1037 Method References

- 1038 71. Beccari, L. *et al.* Generating Gastruloids from Mouse Embryonic Stem Cells.
1039 *Protoc Exch* 1–8 (2018) doi:10.1038/protex.2018.094.
- 1040 72. Vianello, S., Girgin, M., Rossi, G. & Lutolf, M. Protocol to immunostain
1041 Gastruloids (LSCB, EPFL). *Protocols.io* 1–10 (2020).
- 1042 73. Andrey, G. *et al.* Characterization of hundreds of regulatory landscapes in
1043 developing limbs reveals two regimes of chromatin folding. *Genome Res* **27**,
1044 223–233 (2017).
- 1045 74. Lee, T. I., Johnstone, S. E. & Young, R. A. Chromatin immunoprecipitation and
1046 microarray-based analysis of protein location. **1**, 729–748 (2006).
- 1047 75. Radzisheuskaya, A. *et al.* Complex-dependent histone acetyltransferase activity
1048 of KAT8 determines its role in transcription and cellular homeostasis. *Mol Cell*
1049 **81**, 1749–1765.e8 (2021).
- 1050 76. Love, M. I., Huber, W. & Anders, S. Moderated estimation of fold change and
1051 dispersion for RNA-seq data with DESeq2. *Genome Biol* **15**, 1–21 (2014).
- 1052 77. Yu, G., Wang, L. G., Han, Y. & He, Q. Y. ClusterProfiler: An R package for
1053 comparing biological themes among gene clusters. *OMICS* **16**, 284–287 (2012).
- 1054 78. Langmead, B. & Salzberg, S. L. Fast gapped-read alignment with Bowtie 2. *Nat
1055 Methods* **9**, 357–359 (2012).
- 1056 79. Li, H. *et al.* The Sequence Alignment/Map format and SAMtools. *Bioinformatics*
1057 **25**, 2078–2079 (2009).
- 1058 80. Tarasov, A., Vilella, A. J., Cuppen, E., Nijman, I. J. & Prins, P. Sambamba: Fast
1059 processing of NGS alignment formats. *Bioinformatics* **31**, 2032–2034 (2015).
- 1060 81. Fursova, N. A. *et al.* Synergy between Variant PRC1 Complexes Defines
1061 Polycomb-Mediated Gene Repression. *Mol Cell* **74**, 1020–1036.e8 (2019).
- 1062 82. Ramírez, F., Dündar, F., Diehl, S., Grüning, B. A. & Manke, T. DeepTools: A flexible
1063 platform for exploring deep-sequencing data. *Nucleic Acids Res* **42**, 187–191
1064 (2014).
- 1065 83. Robinson, J. T., Thorvaldsdóttir, H., Turner, D. & Mesirov, J. P. igv.js: an
1066 embeddable JavaScript implementation of the Integrative Genomics Viewer
1067 (IGV). *Bioinformatics* **39**, 23–24 (2023).
- 1068 84. Kerpedjiev, P. *et al.* HiGlass: Web-based visual exploration and analysis of
1069 genome interaction maps. *Genome Biol* **19**, (2018).

- 1070 85. Zhang, Y. *et al.* Model-based Analysis of ChIP-Seq (MACS). *Genome Biol* **9**, R137
1071 (2008).
- 1072 86. Ross-Innes, C. S. *et al.* Differential oestrogen receptor binding is associated with
1073 clinical outcome in breast cancer. *Nature* **481**, 389–393 (2012).
- 1074 87. Yu, G., Wang, L. G. & He, Q. Y. ChIP seeker: An R/Bioconductor package for ChIP
1075 peak annotation, comparison and visualization. *Bioinformatics* **31**, 2382–2383
1076 (2015).
- 1077 88. Chronis, C. *et al.* Cooperative Binding of Transcription Factors Orchestrates
1078 Reprogramming. *Cell* **168**, 442–459.e20 (2017).
- 1079 89. Servant, N. *et al.* HiC-Pro: An optimized and flexible pipeline for Hi-C data
1080 processing. *Genome Biol* **16**, (2015).
- 1081 90. Abdennur, N. & Mirny, L. A. Cooler: Scalable storage for Hi-C data and other
1082 genomically labeled arrays. *Bioinformatics* **36**, 311–316 (2020).
- 1083 91. Yang, T. *et al.* HiCRep: assessing the reproducibility of Hi-C data using a stratum-
1084 adjusted correlation coefficient. *Genome Res* **27**, 1939–1949 (2017).
- 1085 92. Imakaev, M. *et al.* Iterative correction of Hi-C data reveals hallmarks of
1086 chromosome organization. *Nat Methods* **9**, 999–1003 (2012).
- 1087 93. Roayaei Ardashany, A., Gezer, H. T., Lonardi, S. & Ay, F. Mustache: Multi-scale
1088 detection of chromatin loops from Hi-C and Micro-C maps using scale-space
1089 representation. *Genome Biol* **21**, 1–17 (2020).
- 1090 94. Flyamer, I. M., Illingworth, R. S. & Bickmore, W. A. Coolpup.py: Versatile pile-up
1091 analysis of Hi-C data. *Bioinformatics* **36**, 2980–2985 (2020).
- 1092 95. Quinlan, A. R. & Hall, I. M. BEDTools: A flexible suite of utilities for comparing
1093 genomic features. *Bioinformatics* **26**, 841–842 (2010).
- 1094 96. Kremer, K. & Grest, G. S. Dynamics of entangled linear polymer melts: A
1095 molecular-dynamics simulation. *J Chem Phys* **92**, 5057–5086 (1990).
- 1096 97. Di Stefano, M., Paulsen, J., Lien, T. G., Hovig, E. & Micheletti, C. Hi-C-constrained
1097 physical models of human chromosomes recover functionally-related properties
1098 of genome organization. *Sci Rep* **6**, 1–12 (2016).
- 1099 98. Plimpton, S. Fast Parallel Algorithms for Short-Range Molecular Dynamics. *J
1100 Comput Phys* **117**, 1–19 (1995).
- 1101 99. Ghosh, S. K. & Jost, D. How epigenome drives chromatin folding and dynamics,
1102 insights from efficient coarse-grained models of chromosomes. *PLoS Comput
1103 Biol* **14**, 1–26 (2018).
- 1104 100. Gu, B. *et al.* Transcription-coupled changes in nuclear mobility of mammalian
1105 cis-regulatory elements. *Science (1979)* **359**, 1050–1055 (2018).
- 1106 101. Humphrey, W., Dalke, A. & Schulten, K. VMD: Visual molecular dynamics. *J Mol
1107 Graph* **14**, 33–38 (1996).

1108 1109 Data Availability

1110 All raw data were submitted to the National Library of Medicine's (NCBI) Sequence Read
1111 Archive (SRA) and the processed files were submitted to the Gene Expression Omnibus
1112 (GEO). All data can be retrieved under the GEO SuperSeries GSE281151. Micro-C pairing
1113 statistics are detailed in Supplementary Table 1. Differential gene expression and differential

1114 chromatin looping results can be found in Supplementary Table 2. ChIP-seq, RNA-seq and
1115 loop anchor Gene Ontology enrichment can be found in Supplementary Table 3.

1116

1117 **Code Availability**

1118 Scripts used for biophysical modelling in this article are available at
1119 https://github.com/cavallifly/Paldi_et_al_2024.

1120

1121 **Acknowledgements**

1122 We thank Ivana Jerkovic and Frederic Bantignies for comments on the manuscript. We are
1123 grateful to Dovetail Genomics (Cantata Bio) for their contribution to Micro-C reagent costs. We
1124 are grateful to the Genotoul bioinformatics platform Toulouse Occitanie
1125 (BioinfoGenotoul, <https://doi.org/10.15454/1.5572369328961167E12>) and the Pôle
1126 Scientifique de Modélisation Numérique (PSMN) of the ENS de Lyon for computational
1127 resources. We thank the Montpellier Resources Imagerie (MRI) for their help and support with
1128 microscopy. FP was supported by HFSP Long-term Fellowship LT000111/2021-L and EMBO
1129 Long-term Fellowship ATLF 716-2020. MS was supported by a Marie Skłodowska-Curie
1130 Innovative Training Network (grant no. 813327 ‘ChromDesign’) and Fondation de
1131 Recherche Medicale. HR was supported by La Ligue Contre le Cancer. This work in the
1132 Cavalli lab was funded through grants from the European Research Council (Advanced Grant
1133 3DEpi), from the “Agence Nationale pour la Recherche” (EpiGenMed ANR-10-LABX-12-01;
1134 PLASMADIFF3D, grant N. ANR-18-CE15-0010, LIVCHROM, grant N. ANR-21-CE45-0011),
1135 by the European E-RARE NEURO DISEASES grant “IMPACT”, by the Fondation ARC
1136 (EpiMM3D), by the Fondation pour la Recherche Médicale (EQU202303016280), by the MSD
1137 Avenir Foundation (Project GENE-IGH), and by the French National Cancer Institute (INCa,
1138 PIT-MM grant N. INCA-PLBIO18-362).

1139

1140 **Contributions**

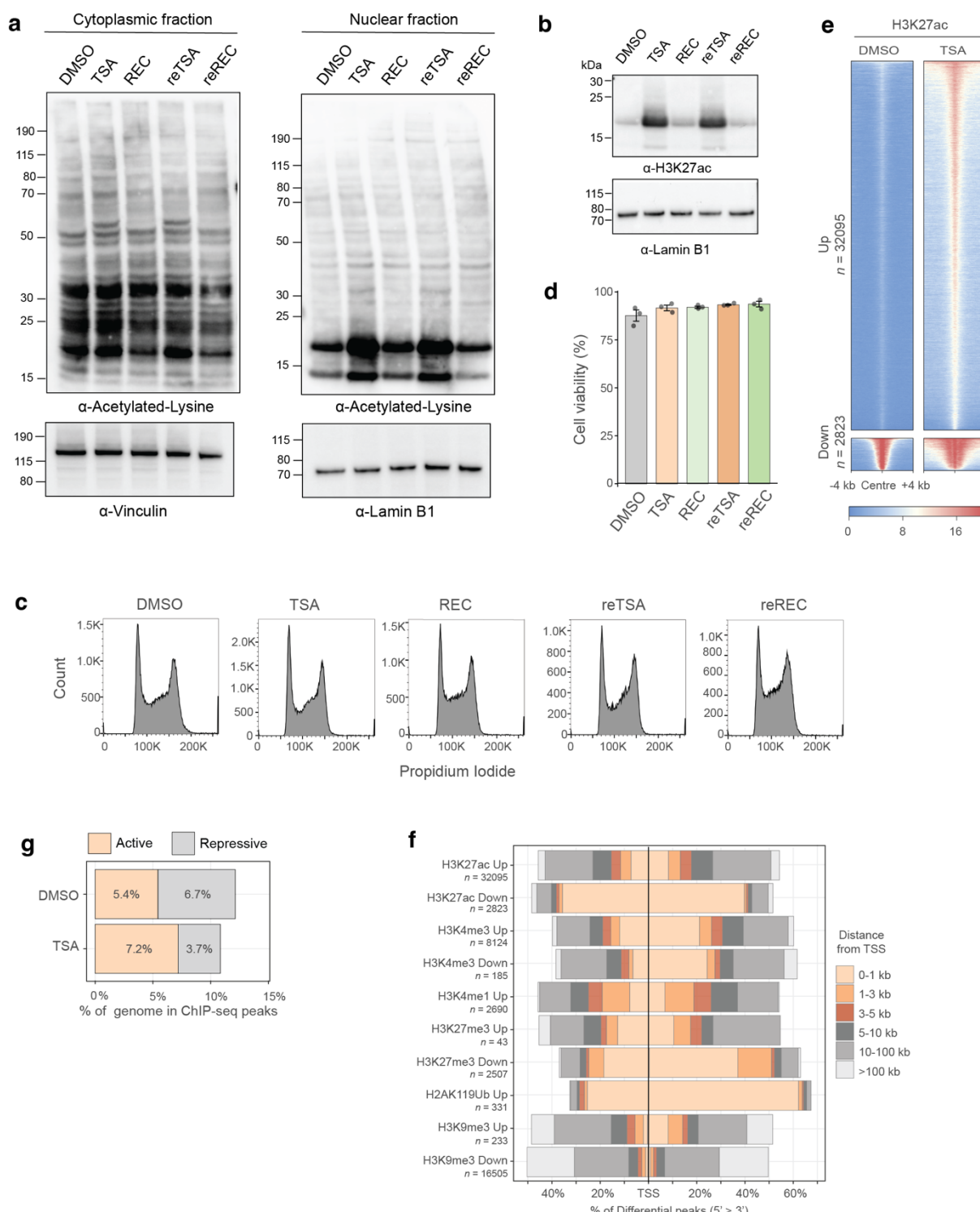
1141 GC and FP conceived the study. GC supervised the project and FP designed and carried out
1142 wet-lab experiments and analysed all data. MS optimised gastruloid culture, and helped to
1143 carry out FACS, ChIP-seq and ATAC-seq experiments as well as Micro-C data analysis. MDS
1144 and DJ designed biophysical modelling. MDS carried out polymer simulations and analysis.
1145 HR performed YY1 ChIP-seq. FP wrote the manuscript with input from all authors.

1146

1147 **Competing Interests**

1148 The authors declare no competing interests.

1149



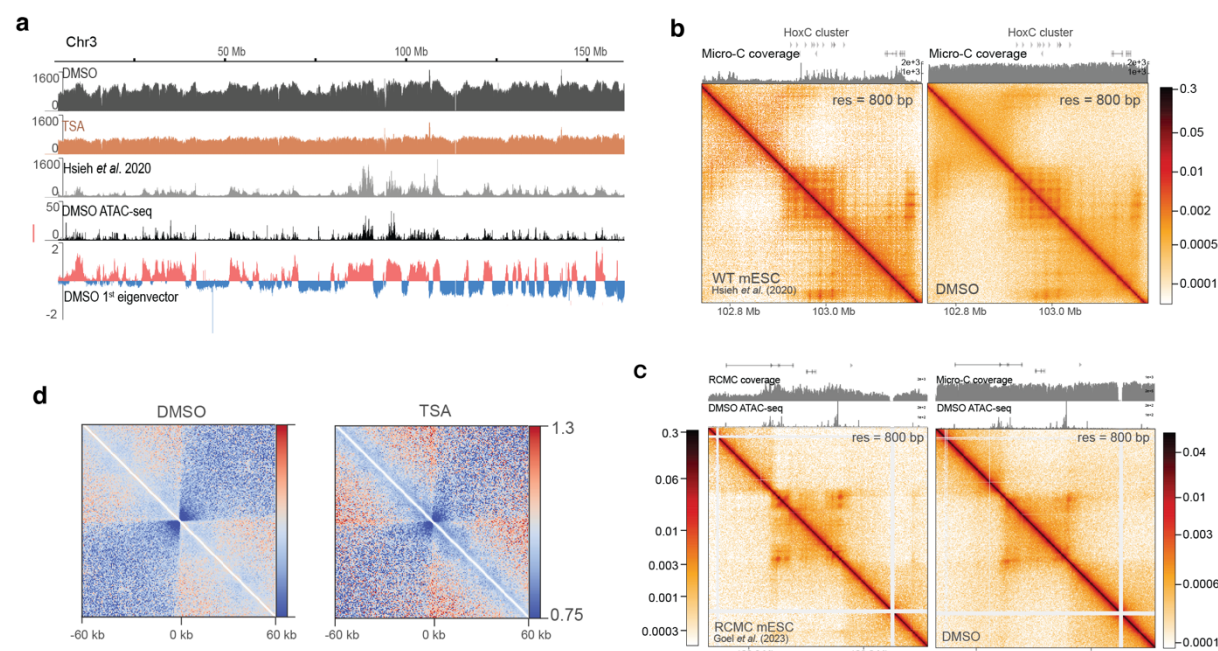
1150

1151 **Extended Data Figure 1 - Characterisation of the effect of TSA treatment on H3K27ac**
 1152 **levels and histone modification landscape in ESCs.** **a**, Western blots showing the levels of
 1153 lysine acetylation in cytoplasmic (left panels) and nuclear (right panels) extracts in the following
 1154 conditions: DMSO control, TSA treatment, 24-hour recovery following TSA washout (REC),
 1155 sequential TSA treatment (reTSA) and 24-hour recovery from the second TSA treatment
 1156 (reREC). Vinculin and Lamin B1 are used as loading control for cytoplasmic and nuclear

1157 samples respectively. **b**, Western blot showing the levels of H3K27 acetylation in nuclear
1158 extracts in conditions as in **a**. Lamin B1 is used as loading control. **c**, Cell cycle analysis by
1159 flow cytometry using propidium iodide in conditions as in **a**. **d**, Cell cycle viability counts in
1160 conditions as in **a**. Mean of three biological replicates \pm s.e.m **e**, Heat maps showing H3K27ac
1161 ChIP-seq signal at differential peaks. **g**, Bar plots showing percentage of the genome in ChIP-
1162 seq peaks of active and repressive histone marks. **f**, Bar plots showing the distance of
1163 differential ChIP-seq peaks (H3K27ac, H3K4me3, H3K4me1, H3K27me3, H2AK119Ub,
1164 H3K9me3) from transcription start sites (TSS).

1165

1166

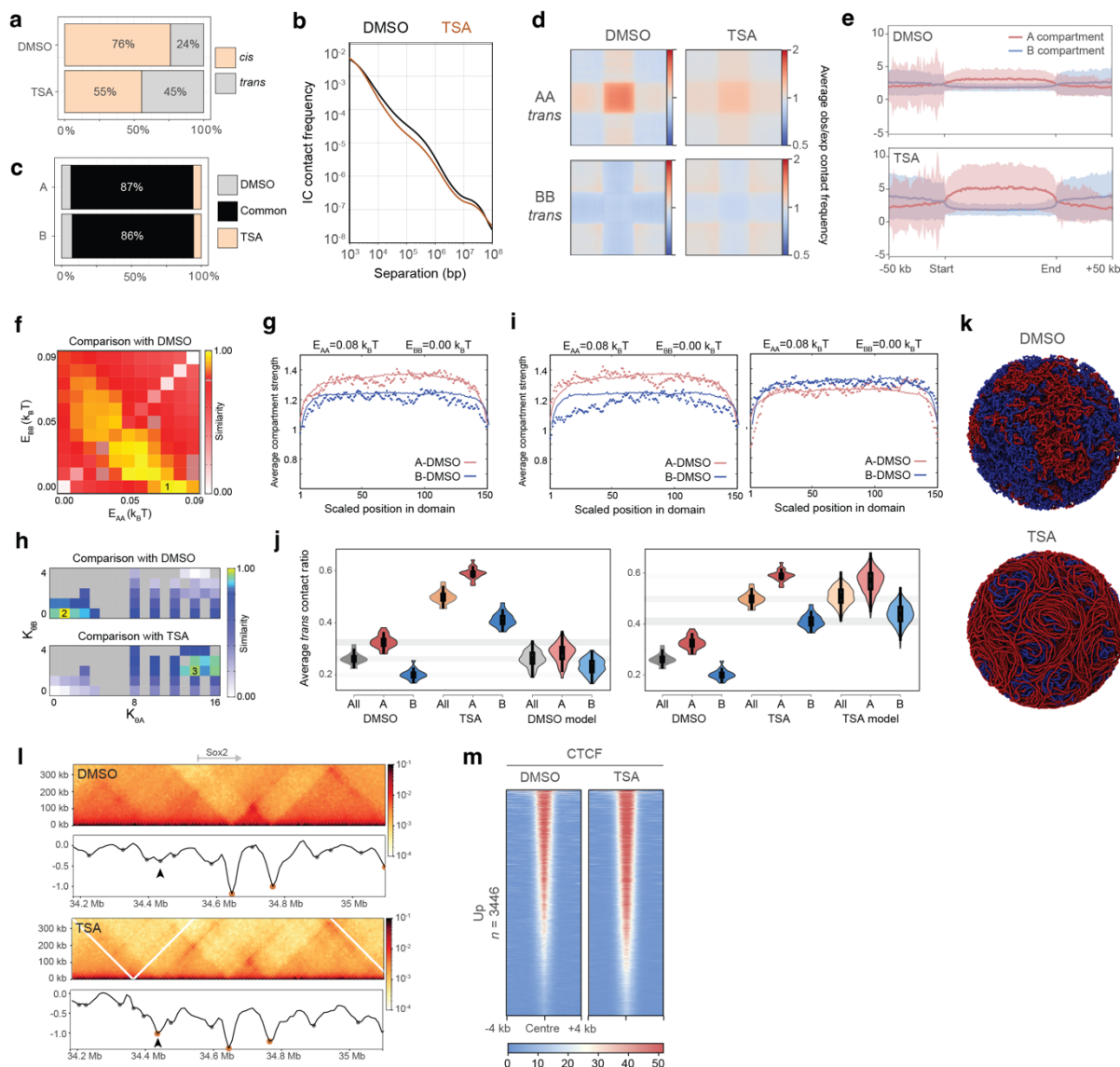


1167

1168

1169 **Extended Data Figure 2 – Micro-C data coverage.** **a**, Total Micro-C coverage in DMSO,
1170 TSA, data from Hsieh et al. (2020) on chromosome 3, along with ATAC-seq signal and
1171 eigenvector tracks in DMSO. **b**, Micro-C maps showing contacts over the HoxC cluster in WT
1172 mESCs (Hsieh et al. 2020) and in DMSO. Corresponding Micro-C coverage tracks are
1173 displayed above the maps. **c**, Region Capture Micro-C (RCMC) map (left) and Micro-C map
1174 (right) from this study showing contacts over the HoxC cluster in WT mESCs (Goel et al. 2023)
1175 and in DMSO. RCMC data has been downsampled to match depth of the Micro-C map in the
1176 capture region. Corresponding RCMC or Micro-C coverage tracks are displayed above the
1177 maps. **d**, On-diagonal pile-ups centred at microcompartment loop anchors identified by Goel
1178 et al. (2023) at the Klf1, Sox2 and Nanog loci (resolution = 600 bp).

1179



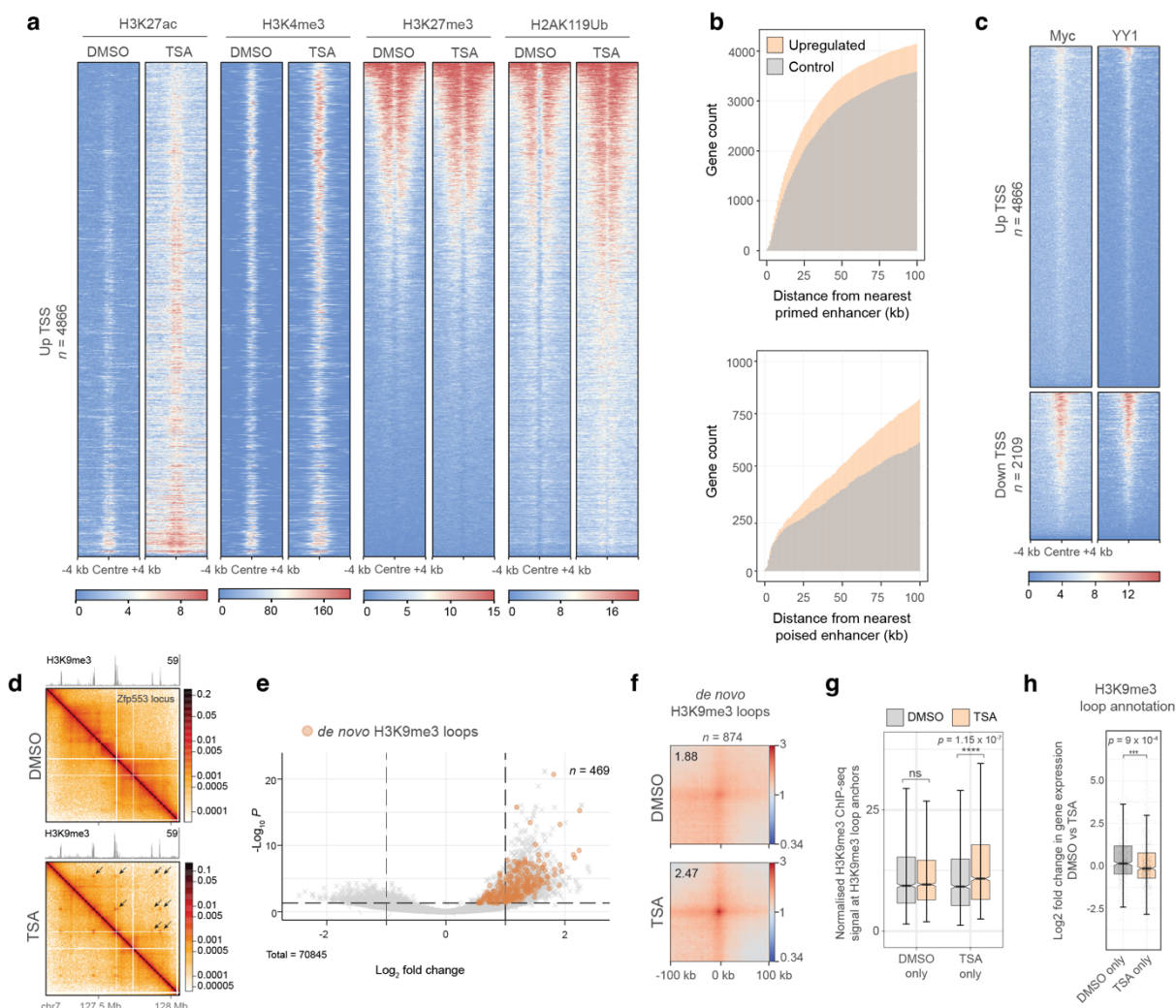
1180

1181

1182 **Extended Data Figure 3 – The effect of HDAC inhibition on genome folding.** **a**, Ratio of
1183 cis versus trans contacts in Micro-C datasets. **b**, Micro-C contact frequency plotted against
1184 genomic separation representing cis decay. **c**, Proportion of unique versus common genomic
1185 regions assigned to A and B compartments in DMSO and TSA. **d**, Aggregate plots of
1186 homotypic interactions between and A and B compartments in trans. **e**, Metaplots showing
1187 H3K4me1 ChIP-seq read density over A and B compartments (bin size = 1 kb). Shading
1188 represents standard deviation. **f**, Heatmap of the similarity scores between the compartment-
1189 strength (CS) profiles in DMSO Micro-C and the models for different parameter sets (E_{AA}, E_{BB}).
1190 **g**, A- and B-specific CS profiles from DMSO Micro-C data (lines) and single-chain simulations
1191 with optimised attraction energies (points). **h**, Heatmap of the similarity scores between the
1192 median of the chromosome-averaged trans-contact ratio (TR) in DMSO and TSA Micro-C
1193 datasets and the models for different parameter sets ($K_{\theta A}, K_{\theta B}$). The compartment-specific

1194 attraction energies (E_{AA}, E_{BB}) were maintained equal to the single-chain optimised values. Gray
 1195 entries indicate untested parameter sets. **i**, Distribution of the *trans*-contact ratios per
 1196 chromosome in DMSO and TSA Micro-C data, and the optimal models for DMSO (left) and
 1197 TSA (right). **j**, Distribution of the TR in optimized models for DMSO (left) and TSA (right). No
 1198 further optimisation of the compartment-specific attractions (E_{AA}, E_{BB}) was performed to
 1199 generate the model profiles in TSA (right). Shading represents inter-quartile range. **k**, Example
 1200 configurations of modelled nuclei corresponding to DMSO (top) and TSA (bottom) conditions.
 1201 Red beads represent A compartments, blue beads represent B compartments. **l**, Micro-C
 1202 maps and insulation curves showing a new TAD boundary forming at the Sox2 locus upon
 1203 TSA treatment (resolution = 10 kb). **m**, Heat maps showing CTCF ChIP-seq signal at
 1204 differential peaks.

1205



1206

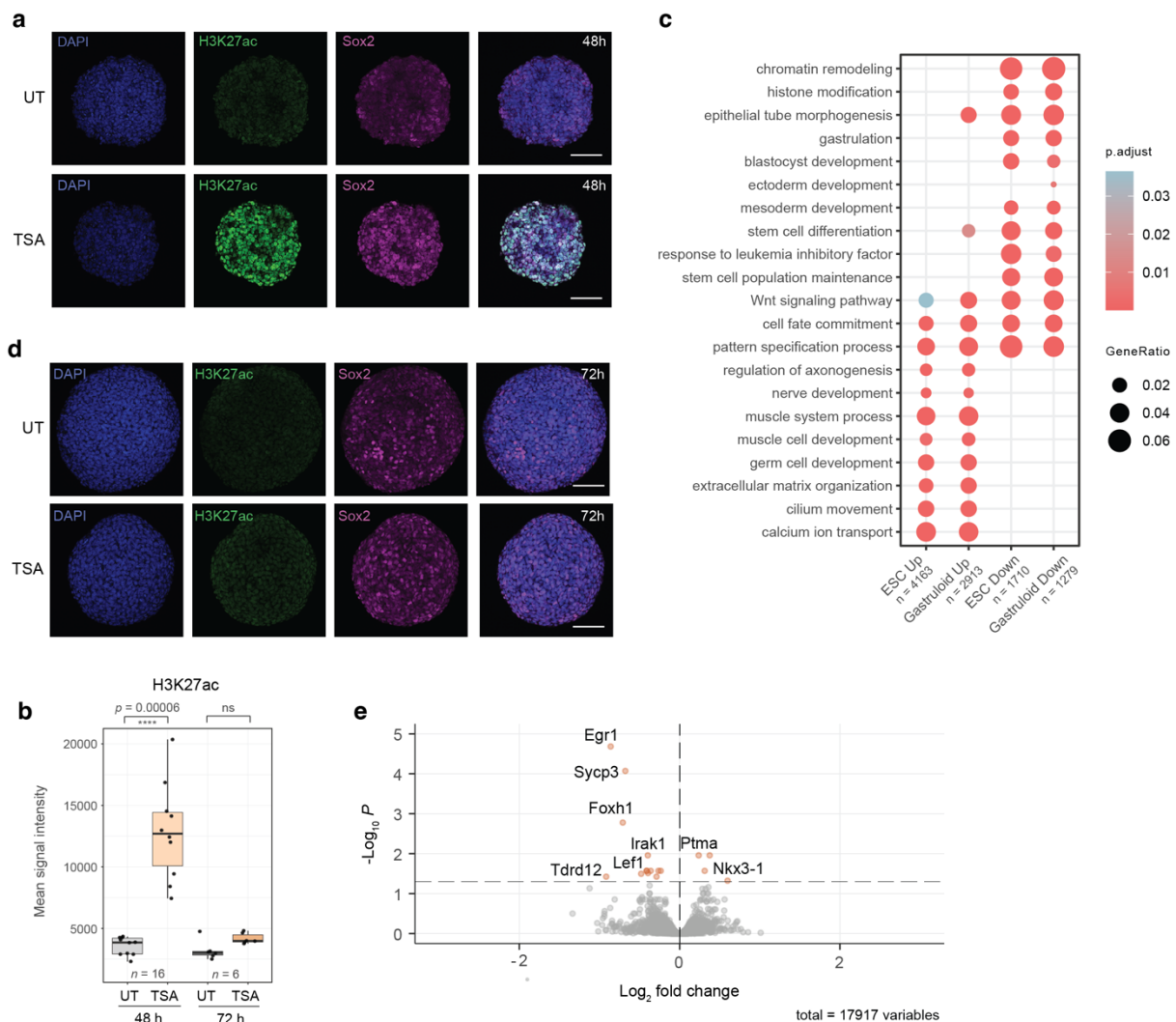
1207

1208 **Extended Data Figure 4 – Chromatin changes in TSA near deregulated TSSs.** **a**,
 1209 Heatmaps showing H3K27ac, H3K4me3, H3K27me3 and H2AK119Ub signal in DMSO and
 1210 TSA around transcription start sites (TSS) of upregulated genes. **b**, Cumulative histogram

1211 showing genomic distance between upregulated gene promoters and the nearest primed
1212 (upper panel) or poised (lower panel) enhancer. Control genes represent an expression-
1213 matched gene set that does not increase in expression. **c**, Heatmaps showing Myc and YY1
1214 ChIP-seq signal around up- and downregulated TSSs. **d**, Contact map showing extensive
1215 H3K9me3-associated differential looping at the Zfp553 locus. Corresponding H3K9me3 signal
1216 is displayed above. **e**, Volcano plot of differential loops between DMSO and TSA with *de novo*
1217 H3K9me3 TSA loops highlighted in orange. Positive log₂ fold change indicates stronger
1218 interaction in TSA. **f**, Pile-up of Micro-C signal (resolution = 4 kb) around *de novo* H3K9me3
1219 loops that form in TSA. **g**, Boxplot showing the normalised H3K9me3 signal at anchors of *de*
1220 *novo* H3K9me3 TSA loops. Data shown are the median, with hinges corresponding to
1221 interquartile range (IQR) and whiskers extending to the lowest and highest values within 1.5×
1222 IQR, notch shows 95% confidence interval (CI) (unpaired two-tailed t-test; ns > 0.05, ****p <
1223 0.0001). **h**, Log₂ fold change in gene expression (TSA vs DMSO) of genes that are nearest
1224 DMSO-only or TSA-only loop anchors. Data shown are the median, with hinges corresponding
1225 to IQR and whiskers extending to the lowest and highest values within 1.5× IQR, notch shows
1226 95% CI (unpaired two-tailed t-test; ns > 0.05, **p < 0.01).

1227

1228

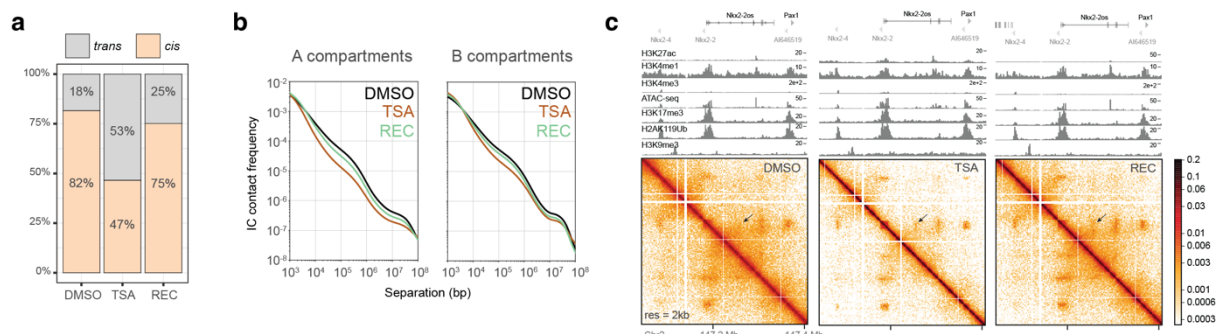


1229

1230

1231 **Extended Data Figure 5 – HDAC inhibition-induced chromatin and gene expression**
1232 **changes in mESC and gastruloids.** **a**, Representative images of H3K27ac and Sox2
1233 immunostaining in 48-hour gastruloids with (bottom) or without (top) TSA treatment (scale bar
1234 = 100 μ m). **b**, Quantification of H3K27ac (left panel) and Sox2 (right panel) signal intensities
1235 in early (48 h, 72 h) gastruloids with and without TSA treatment. Data shown are the median,
1236 with hinges corresponding to IQR and whiskers extending to the lowest and highest values
1237 within 1.5 \times IQR. **c**, Gene Ontology enrichment of terms related to development among
1238 differentially expressed genes in mESCs and 48-hour gastruloids after 4 hours of TSA
1239 treatment. **d**, Representative images of H3K27ac and Sox2 immunostaining in 72-hour
1240 gastruloids with (bottom) or without (top) TSA treatment (scale bar = 100 μ m). **e**, Volcano plot
1241 showing differentially expressed genes in 120-hour gastruloids with versus without TSA
1242 treatment (significance cutoff: adjusted p-value > 0.05) Positive log₂ fold change signifies
1243 upregulation in TSA-treated gastruloids.

1244

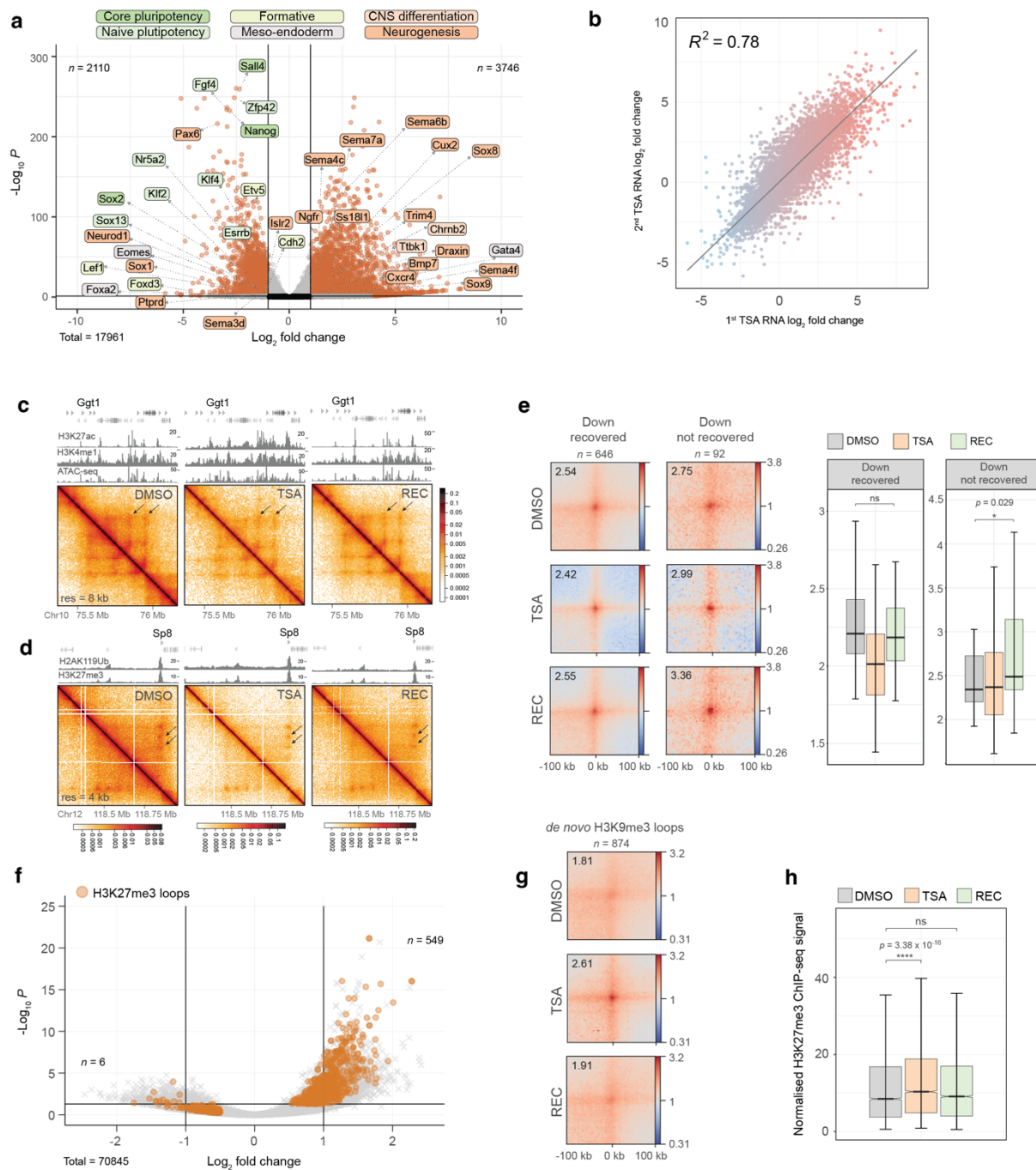


1245

1246

1247 **Extended Data Figure 6 – Reversibility of HDAC inhibition-induced architectural**
1248 **changes. a**, Ratio of *cis* versus *trans* contacts in Micro-C datasets. **b**, Contact frequency in
1249 Micro-C plotted against genomic separation representing *cis* decay by compartment. **c**, Micro-
1250 C maps at the Nkx2-2 locus showing incomplete architectural recovery. ChIP-seq tracks of the
1251 corresponding condition are shown above.

1252



1263 signal are displayed above. **d**, Contact map showing Polycomb-mediated contacts at the Sp8
1264 locus that shows sustained transcriptional downregulation. Corresponding H2AK119Ub and
1265 H3K27me3 signal are displayed above. **e**, Aggregate plots of Micro-C signal around loops
1266 where anchors overlap with downregulated TSSs that recover (left panes) or do not recover
1267 (right panels) (resolution = 4 kb). Quantification of piled-up loop signal is shown on the
1268 right (paired two-tailed t-test; ns > 0.05, ***p < 0.001). Data shown are the median, with hinges
1269 corresponding to IQR and whiskers extending to the lowest and highest values within 1.5×
1270 IQR. **f**, Volcano plot of differential loops between DMSO and TSA. H3K27me3 loops are
1271 highlighted in orange. Positive log₂ fold change indicates stronger interaction in TSA. **g**, Pile-
1272 up of Micro-C signal (resolution = 4 kb) around *de novo* H3K9me3 loops that form in TSA. **h**,
1273 Boxplot showing the normalised H3K27me3 signal at anchors of H3K27me3 loops in DMSO,
1274 TSA and Recovery. Data shown are the median, with hinges corresponding to IQR and
1275 whiskers extending to the lowest and highest values within 1.5× IQR (unpaired two-tailed t-
1276 test; ns > 0.05, ***p < 0.001).

1277